Meteoric ^{10}Be reveals a young, active accretionary prism and structurally complex décollement in the vicinity of the 2011 Tohoku earthquake rupture

Christine Regalla [1*], Paul Bierman[2], and Dylan H. Rood[3]

[1]Boston University Department of Earth and Environment, Boston, MA USA.

*Now at: Northern Arizona University School of Earth and Sustainability, Flagstaff, AZ.

[2]University of Vermont Department of Geology, Burlington, VT USA.

[3]Imperial College London Department of Earth Science and Engineering, London UK.

Corresponding author: Christine Regalla (christineregalla@gmail.com)

Key Points:

- Meteoric ^{10}Be provides high resolution age control in the frontal prism of the Japan trench at IODP Exp 343 (JFAST) Site C0019.
- The frontal prism and plate boundary contain faults at decameter scale spacing, possibly due to subduction of horst and graben topography.
- The majority of incoming sediments at this location have been accreted to the overriding plate during at least the Quaternary period.

Abstract

We present new meteoric ^{10}Be concentration data from marine sediment cores recovered during International Ocean Drilling Program Expedition 343 (JFAST) that help constrain the age, origin, and internal structure of the frontal prism at the Japan trench in the vicinity of the 2011 Tohoku-oki M9 earthquake rupture. ^{10}Be sediment ages from the lower portion of the frontal prism range from ~0-10 Ma, with >60% of analyzed samples above the décollement yielding young ages <2 Ma. Repetition and inversion of high-over-low ^{10}Be-concentration sediments indicate the presence of stratigraphic inversions that correspond to faulting and imbrication of late Miocene and Quaternary sediments. The density of faults inferred indicate that the frontal prism has a fault spacing on the order of 10s of meters, and the identification of faults in the underthrust section suggests the plate boundary décollement may be a zone with multiple slip surfaces. Comparison of ^{10}Be concentrations in the frontal prism with those of the incoming and forearc slope sediments indicates that the majority of the prism is sourced from accretion of Pacific plate sediments, rather than from reworked frontal prism or slope sediments. These data suggest that over at least the past ~1-2 Ma, the décollement preferentially has localized at or near the base of the incoming sediment section, with relatively efficient sediment accretion occurring even in the presence of subducted horst and graben topography.

Plain Language Summary

We help constrain the physical and mechanical properties of the materials near the trench that hosted the 2011 Tohoku M9 earthquake and tsunami, and test whether sediments from the Pacific Plate are scraped off or subducted as they enter the subduction zone. We use sediments from cores recovered during the International Ocean Drilling Program Expedition 343. Because traditional sedimentologic and biostratigraphic techniques alone are not sufficient to determine sediment source region, we apply a new approach using the radio-decay of the ^{10}Be isotope. We use ^{10}Be to date sediments, to identify sediments that have been faulted out of chronologic order, and to correlate sediments between sites. Our results show numerous faults in the system, likely resulting from multiple stages of deformation during slip over rough seafloor topography. Our data also indicate that 50-90% of the sediments on the incoming Pacific Plate are scraped off, and 10-50% of the incoming sediments are subducted. The subducted sediments consist of muds and frictionally weak clays that might promote slip during subduction earthquakes. Similar approaches may provide insight on the composition and evolution of faults that host large earthquakes and tsunami at other plate boundaries.

1. Introduction

The relative roles of accretion, subduction, and tectonic erosion of materials at subduction trenches are a primary control on the volume and composition of the sedimentary inputs into the subduction zone. These processes have important implications for both the mechanical properties of the plate boundary at seismogenic depths (e.g., Morgan et al., 2007; Ruff, 1989; Saffer & Bekins, 2006; Underwood, 2007) and for the long-term mass balance of crustal rocks in the subduction system (e.g., Clift & Vannucchi, 2004; Scholl et al., 1980; von Huene & Scholl, 1991). Input sediments that escape accretion become the materials available to host fault zones in the shallow portion of the subduction systems. The evolution of mineral chemistry, sediment mechanics, fluid pressures, and fault geometries within these subducted materials influence the ability for earthquake ruptures to propagate to the sea floor (e.g. Saffer and Tobin, 2011; Underwood, 2007). Sediments that are accreted contribute to the growth of continental crust. The Japan trench (Fig. 1) has been conventionally considered a type example of a margin experiencing nearly complete sediment subduction and mass loss through tectonic erosion, with little to no net accretion over the Miocene to present (e.g., Kimura et al., 2012; von Huene & Culotta, 1989; R. von Huene & Lallemand, 1990). However, recently-collected high-resolution, multichannel seismic lines across the Japan trench challenge the conventional view and show that, in many locations, the décollement is localized near the base of the incoming sediment section, and that the overlying sediments on the incoming plate are locally imbricated and accreted to the frontal prism (Fig. 2) (Chester et al., 2013; Nakamura et al., 2013). These data suggest that sediment accretion, rather than sediment subduction or erosion, may be the dominant mode of mass transfer in the Japan trench. Such contrasting models make different predictions for the material properties and structural evolution of a portion of the shallow décollement known to host large magnitude (>50 m) tsunamigenic slip to the trench (e.g., Lay et al., 2011).

Several factors complicate our ability to determine shallow décollement geometry and quantify sediment fluxes into the subduction zone in the Japan trench. First, the frontal prism becomes seismically chaotic within a few kilometers landward of the trench, and the incoming stratigraphy cannot be easily traced into the frontal prism (Fig. 2c, Kodaira et al., 2017; Nakamura et al., 2013). The prism, therefore, does not contain reflectors that clearly indicate the orientation of bedding or faults. Second, given the large water depths of the Japan trench (>7 km), material recovered from the frontal prism is hampered by poor core recovery and limited preservation of key indicator fossils that can provide a robust age-depth profile. Third, biogenic muds recovered from the frontal prism are lithologically similar to biogenic muds in both the incoming and forearc slope sediment sequences, making the provenance of these materials unclear (Fig. 2b, Expedition 343/343T Scientists, 2013; Nakamura et al., 2013;). Fourth, the subduction of horst and graben topography on the incoming Pacific plate has the potential to promote spatially complex deformation, slope failure, and slumping that can disrupt prism and shallow décollement evolution (e.g., Koge et al., 2018). Deconvolving the internal architecture and tectonic origin of the frontal prism in the Japan trench requires multiple proxies that can be integrated with existing core, log, and seismic data sets.

To address these challenges, we use meteoric ^{10}Be measured in sediment cores across the frontal prism and plate boundary décollement recovered during International Ocean Drilling Program (IODP) Expedition 343 (Japan Fast Drilling Project, or JFAST) to investigate the age, origin, and structural evolution of the frontal prism in the Japan trench (Fig 1). This approach uses the radiogenic decay of meteoric ^{10}Be as a tool to determine relative and absolute sediment ages, and the concentrations of meteoric ^{10}Be to identify faulted sequences where sediment ages are stratigraphically out of order (c.f. Morris, Valentine, et al., 2002). The high spatio-temporal resolution of sediment ages provided by ^{10}Be allows for the identification of stratigraphic repetitions and omissions across known faults and also can be used to identify new faults not recovered in cores. In addition, by comparing ^{10}Be abundances in the frontal prism to reference ^{10}Be profiles in the forearc slope and incoming plate sediment sequences (Morris, Valentine, et al., 2002), these data can be used to constrain the origin and accretion history of the frontal prism. The ^{10}Be abundances in the incoming and overriding plate sediments, when compared to ^{10}Be profiles in the frontal prism, provide evidence for abundant sediment accretion in the Japan trench over at least the past ~1-2 Ma.

These ^{10}Be isotopic data provide constraints on sediment fluxes, décollement lithology, and décollement evolution for a portion of the shallow plate boundary décollement in the Japan trench that overlaps with the rupture patch of the 2011 Tohoku earthquake (Fig 1). In particular, these data help place constraints on the volume and composition of subducted sediments that may host the plate boundary décollement, particularly within the shallow portion of the plate boundary that experienced seismogenic slip to the trench during the 2011 Tohoku earthquake (e.g., Lay et al., 2011). In addition, these isotopic data help demonstrate that the décollement zone and underthrust sediments in the near trench region contain a network of faults that may each host a component of potentially seismogenic plate boundary slip.

2. Frontal prism evolution as a function of décollement geometry and seafloor topography

Unlike other margins with a thick (>1-3 km), sandy, incoming sediment section that is accreted and imbricated to form a wide (~30-60 km), young, frontal accretionary prism (e.g. Nankai, Cascadia, Barbados), the Japan trench has a thin (~50-300 m) biogenic mud and clay rich incoming sediment section offset by numerous outer rise normal faults, and a narrow (~10-30 km from the trench axis) seismically-chaotic frontal prism (Kodaira et al., 2017; Nakamura et al., 2013) that is overlain by biogenic muds of the forearc slope basin (Fig. 2). The age, origin, and internal structure of the frontal prism are poorly known, but it has been proposed to have evolved as a result of gravitational and tectonic reworking of old Cretaceous to Miocene prism materials and Paleocene to Miocene forearc slope sediments along a margin dominated by mass loss through tectonic erosion, rather than by sediment accretion (e.g., von Huene & Culotta, 1989).

The frontal prism and décollement in the Japan trench could evolve through a range of endmember scenarios (Fig 3). In a simplified system, these endmembers involve: complete sediment accretion, complete sediment subduction, or a mixture of the two. If 100% of the incoming sediment section were accreted, the frontal prism would consist of imbricate thrust repetitions, and the plate boundary décollement would develop in material located at the sediment-basement contact (Fig. 3a). If only part of the sediment section were accreted, the décollement would localize within the subducted sediment section (Fig. 3b). If the complete sediment section were subducted, the décollement would develop at the top of the incoming sediment sequence, and the frontal prism must consist of older forearc slope basin sediments or relict forearc crust (Fig. 3c).

The subduction of horst and graben topography, however, complicates these simplified endmember scenarios (Fig. 3 d-f). The margin may experience partial accretion, partial subduction, or loss of upper plate material (tectonic erosion) depending on the stratigraphic location of the plate boundary décollement relative to the geometry of the incoming plate (presence or absence of horsts and grabens). In this system, nearly complete sediment accretion can only occur if the décollement has an undulating geometry that steps up and over horst and graben topography (Fig 3d). Once accreted, frontal prism sediments experience internal thickening and thrust faulting as the wedge is translated over horsts, and extensional faulting and slumping as the prism is translated over grabens.

Sediment subduction and tectonic erosion can occur if the décollement maintains a relatively planar geometry during the subduction of horst and graben seafloor topography (Fig. 3e and f). In these cases, the relative magnitudes of sediment accretion, subduction, and erosion are a function of décollement position relative to the top of basaltic crust within horsts and grabens. For example, if a planar décollement develops at the top of subducting horsts, sediment accretion may occur only atop subducted horsts, with sediment subduction occurring within grabens (Fig. 3e). Alternately, if the décollement localizes at the top of the sediment section, forearc sediment slumps can fill in the subducting graben, leading to complete sediment subduction and tectonic erosion (Fig. 3f). In this case, if the décollement propagates over the trench fill, both subduction of incoming plate sediment and tectonic erosion of frontal prism sediment are promoted.

3. ^{10}Be Background, Methods, and Data

3.1. *^{10}Be as a tool to evaluate frontal prism evolution*

In the Japan trench, the chaotic nature of seismic data within the frontal prism and the lithologic homogeneity of the biogenic muds that comprise the majority of the incoming and forearc slope sediments make it difficult to distinguish between the potential modes of décollement geometry and forearc evolution without the use of other proxies. We utilize a new application of meteoric ^{10}Be in marine sediments to test between these endmember models, leveraging the radiogenic decay of ^{10}Be that is deposited with pelagic sedimentation on the sea floor (Fig 4). Meteoric ^{10}Be forms in the atmosphere when cosmogenic rays bombard atomic nuclei of O and N, binds to precipitation and aerosols, and is delivered to the ocean via dryfall and rain fall (e.g., Brown, 1987; Morris, Gosse, et al., 2002). Once delivered to the ocean, ^{10}Be is scavenged from the water column by biogenic opal, clay, carbonate, and organic materials, and is deposited with seafloor sediments (Fig. 4) (Chase et al., 2002; Luo & Ku, 2004; McHargue & Damon, 1991; Raisbeck et al., 1979). The concentration of ^{10}Be at the seafloor with time is a function of the flux of these particles to the seafloor, oceanographic conditions that may change sedimentation rate, and atmospheric cosmogenic nuclides production rate. Once deposited and buried in seafloor sediments, ^{10}Be is relatively immobile at temperatures < 200°C and pH > 5 (Brown et al., 1992; Measures & Edmond, 1983; You et al., 1994). ^{10}Be is a radionuclide that decays to ^{10}B with a half-life ($T_{1/2}$) of 1.36 Ma (Nishiizumi et al., 2007). Given its half-life and high initial concentration in sediment, ^{10}Be is detectable in sediments less than ~8-10 Ma. We leverage these properties of ^{10}Be to quantify the internal structure, age, and origin of the frontal prism in the following three ways.

First, the ^{10}Be concentration profile within a sediment column can be used to determine if material is in stratigraphic order, or if it has been disrupted by faulting. In an undisturbed, continuously and constantly depositing marine sediment section, the concentration of ^{10}Be with depth will decrease exponentially from an initial concentration (N_o) at the surface, to below detection limits at depths (Fig. 5a) (e.g., Morris, Valentine, et al., 2002; Wang et al., 1996) because of radioactive decay. Deviations from this pattern can be used to identify faulted intervals. Thrust repetition of a sediment packages in an accreted sequence will show inversions of low-over-high ^{10}Be concentration sediments (Fig 5b), extensionally faulted sections will show section omissions a step decrease to lower ^{10}Be concentration across faults (Fig. 5c), and overturned sections will show an increase in concentration with depth (Fig 5d). Sediment columns that have experienced erosion or hiatuses during deposition will have step decreases and omissions in ^{10}Be concentration similar to that produced by normal faulting (Fig 5c). Additionally, thrust faults that undulate and cut up and down section, or that offset a previously folded section may generate omissions similar to that of normal faults (Fig. 5c).

Second, the radiogenic decay constant of ^{10}Be can be used to estimate numerical sediment ages if the initial concentration of ^{10}Be is known or can be estimated. This can be achieved two ways, either by assuming that the ^{10}Be concentrations of "zero age" sediments at the seafloor are representative of initial concentration over the entire time period of interest, or by back-calculating initial concentrations from older sediments for which ages are independently known (Fig 4). In addition, ^{10}Be concentrations and radiogenic ages in the frontal prism can be used to infer sediment source regions given that ^{10}Be-concentration profiles differ between incoming sediments and the forearc slope sediments in the northern Japan margin (Morris, Valentine, et al., 2002).

Third, bulk ^{10}Be concentrations in the frontal prism can be used to evaluate the relative roles of sediment accretion versus sediment subduction and tectonic erosion in the frontal prism. If the frontal prism is largely the result of frontal accretion of the incoming Miocene to Quaternary sediment section, as implied by seismic reflection profiles (e.g., Nakamura et al., 2013), the frontal prism should contain an abundance of sediment containing high concentrations of ^{10}Be. If, however, accretion rates are slow, and the frontal prism forms by reworking older prism or forearc slope material, (e.g. von Huene & Culotta, 1989), frontal prism sediments should contain little if any ^{10}Be (Fig. 3).

3.2. Measurement of meteoric ^{10}Be

We measured the concentration of ^{10}Be in 24 samples from the frontal prism at the Japan Trench (Table 1, Fig. 6, and Fig. 7) at IODP Site C0019 Hole E. These samples were recovered from 21 core sections collected between 176 – 186 mbsf and 648 – 837 mbsf at Site C0019. Measurements were performed on 5 cm^3 samples of biogenic muds (Lithologic units II, III, and IV; Fig. 7a) collected at ~10 m intervals, and above and below known faults identified by visual core description and X-ray CT Scans (Expedition 343/343T Scientists, 2013). This sampling interval was chosen to be able to test whether or not major faults observed in the core separated relatively intact sequences of imbricated strata. Meteoric ^{10}Be was isolated from sediment at the University of Vermont Cosmogenic laboratory using a total fusion process modified after Stone (1998). Samples were processed in batches that included one process blank and one internal standard. Approximately 500 mg of finely milled sediment was prepared with KHF_2, $NaSO_4$, and ~ 500 μg ^{9}Be carrier. The sample mixtures were fused in platinum crucibles and leached in Milli-Q (18.2 Mohm) water. Following removal of excess potassium via perchlorate precipitation, beryllium was precipitated as $Be(OH)_2$ gels using NH_4OH and purified using cation column chromatography. Dried beryllium hydroxide samples were loaded into copper cathodes and $^{10}Be/^{9}Be$ ratios were measured at the Scottish Universities Environmental Research Center (SUERC) AMS facility (Xu et al., 2015) and normalized to the NIST standard with an assumed $^{10}Be/^{9}Be$ ratio of 2.79 x 10^{-11}, which is consistent with a ^{10}Be half-life of 1.36 Ma (Nishiizumi et al, 2007). The $^{10}Be/^{9}Be$ ratios we measured were converted to ^{10}Be concentrations using the known masses of sediment and carrier for each sample. Published ^{10}Be concentrations from DSDP sites 434 and 436 were normalized to standards at the time of measurement (Morris, Valentine, et al., 2002). However, those standards and their nominal values were not included in the publication (Morris, Valentine, et al., 2002). Attempts to contact the lead author failed, and the AMS facilities used by the author do not have access to the published samples names. Thus, given uncertainty of the standards and their nominal value, we normalized these published data from 2002 to a range of possible AMS standards (Nishiizumi et al, 2007), and report minimum and maximum bounds for comparison with ^{10}Be data from IODP Expedition 343.

3.3. Determination of ^{10}Be-ages

^{10}Be ages of marine sediment from IODP Site C0019, and DSDP Sites 434 and 436 were determined for λ = 0.5097 Ma ($T_{1/2}$ = 1.36 Ma), by solving the following equation for *t*:

$$N=N_oe^{-\lambda t} \quad \text{(Eq. 1)}$$

We locally calibrate the initial concentration of ^{10}Be (N_o) three ways: a) by calculating N_o from Radiolarian sample C0019E-11R-CC-10.0 cm (786.60 mbsf) and ^{10}Be sample C0019E-11R-CC-3.0 cm (780.56 mbsf) that are co-located in the same core-catcher sample; b) by calculating N_o from Radiolarian sample C0019E-1R-CC-1.0 cm (184.99 mbsf) and ^{10}Be sample C0019E-1R-3-128.0 cm (181.17 mbsf), where the Radiolarian age has the smallest uncertainty of all samples analyzed at site C0019E (4.3-4.4 Ma; Chester et al., 2013); and c) by assuming N_o is equal the ^{10}Be concentration of the youngest sediments in incoming plate reference site 436 (22.8x10^8 atoms/g; Morris, Valentine, et al., 2002). These data yield a range of N_o from 15.8x10^8 to 24.4x10^8 atoms/g. Because N_o of less than 21.7 x10^8 atoms/g yield negative ^{10}Be ages for many samples, we use an N_o of 21.7x10^8 to 24.4x10^8 atoms/g to calculate ^{10}Be ages for all samples from Site C0019. This approach assumes that N_o in seafloor sediments remained within this range over the time period of investigation. Our calculated N_o values are consistent with ^{10}Be concentrations measured in "zero-aged" surface seafloor sediments in the western Pacific outboard of the Japan trench (Ku et al., 1985; Lao et al., 1992; Morris, Valentine, et al., 2002), and those back-calculated from 0-5 Ma sediments cored at DSDP Site 436, suggesting this assumption is valid (Tables 2 and 3).

3.4. ^{10}Be concentrations and sediment ages

The ^{10}Be concentrations measured in sediments recovered from the northeast Japan frontal prism at IODP at Site C0019 range from 0.18x10^8 to 21.9x10^8 atoms/g, and no sediments analyzed had ^{10}Be concentrations below detection limits (Table 1). Duplicate ^{10}Be concentrations measured for repeat samples (343-5-1, 343-8-1A, and 343-18-1) overlap within measurement uncertainty, which is consistently less than 5% (1σ). The range of measured ^{10}Be concentrations in Site C0019 cores is comparable to those previously measured in the forearc slope and incoming sediment sections at DSDP Sites 434 and 436 (1.6×10^{8} to 23.0×10^{8} atoms/g, Morris, Valentine, et al., 2002) (Table 3, Fig. 6).

Ages derived from ^{10}Be concentrations from Site C0019 range from Holocene to Late Miocene (0 – 9.63 Ma) (Table 2, Fig. 6b). Age uncertainty in these samples come from two sources. Analytical uncertainty in ^{10}Be concentrations yield average age uncertainties of 0.03 Ma (2σ). This uncertainty is relevant for comparison of ^{10}Be ages or concentrations to determine the relative age difference between samples. The second, and larger, source of ^{10}Be age uncertainty is the result of uncertainty in N_o, which for this study is 2.7×10^{8} atoms/g, and equates to an ^{10}Be age uncertainty of approximately ±0.2 Ma (2σ). This uncertainty is a more realistic estimate of the uncertainty of the absolute ^{10}Be age of the measured sediment samples. This value of uncertainty is relevant when comparing a ^{10}Be age with other biostratigraphic or geochronologic age constraints. Despite uncertainty in N_o, average uncertainties in ^{10}Be ages are typically smaller than typical uncertainties in biostratigraphic radiolarian ages at this site, which range from 0.1-2.6 Ma (Expedition 343/343T Scientists, 2013).

Measured ^{10}Be ages from Site C0019 Hole E (Table 2) overlap with radiolarian biostratigraphic ages for samples co-located to within 1 m depth in the core (Fig. 7b). Because ^{10}Be concentrations have the ability to provide better relative age control than biostratigraphy, particularly in young (~1-2 Ma) sediments, ^{10}Be can be used to identify fault inversions that would not be resolvable through biostratigraphy alone. Examples of this are seen in C0019 at ~645-660 mbsf, and ~690 to ~730 mbsf, where radiolarian biostratigraphic ages overlap, but variations in ^{10}Be concentration indicate these samples likely have different depositional ages (Fig. 7b).

4. ^{10}Be as a tool to quantify prism age and structure

4.1. Sediment age distribution within the frontal prism

^{10}Be concentration data from Site C0019 indicate that more than 60% of the samples in the lower frontal prism from ~640-820 mbsf above the décollement are high concentration (> 8×10^{8} atoms/g ^{10}Be), young (0 – 2Ma) sediment. In addition, this portion of the prism shows a general increase in ^{10}Be concentration (decrease in age) with depth (Fig. 6b). The sample with the highest ^{10}Be concentration (22×10^{8} atoms/g ^{10}Be, 0.11 Ma) occurs in Core 16R at 819 mbsf (Fig. 7b; Tables 1 and 2), approximately 2 m above the décollement (821.5-822.5 mbsf). The presence of young, high ^{10}Be material at depth in the lower portion of the prism, and the general younging of sediment age with depth is consistent with frontal prism development via frontal accretion, such as depicted in Figs. 3a, b, d and e, but are inconsistent with the predictions of endmember scenarios involving 100% sediment subduction and tectonic erosion (Figs. 3c and f).

The lowest ^{10}Be concentrations (oldest ^{10}Be ages) occur at two depth intervals in C00019. The first interval is within Cores 18R-20R at 825-835 mbsf, below the décollement (Lithologic Unit IV), where samples yield ^{10}Be concentrations of 0.18x10^{8} to 0.73x10^{8} atoms/g and ^{10}Be ages of 6.7-9.5 Ma (Fig. 7b; Tables 1 and 2). The low ^{10}Be concentrations and Miocene ^{10}Be ages observed below the décollement (Figs. 6b and 7b) are consistent with geochemical data that correlate this material to the lowermost 50-100 m of the sedimentary section of the incoming Pacific plate (Expedition 343/343T Scientists, 2013; Kirkpatrick et al., 2015; Rabinowitz et al., 2015). The absence of the uppermost section of the incoming Pacific Plate sediments below the plate boundary décollement at Site C0019 are inconsistent with the predictions of endmember scenarios with 100% sediment subduction and tectonic erosion (Figs. 3c and f).

The second interval with low ^{10}Be concentration sediments is located above the décollement within the frontal prim, in Cores 2R-3R at 645-655 mbsf (Lithologic Unit II), where samples yield ^{10}Be concentrations of 0.24x10^{8} to 1.05x10^{8} atoms/g and ^{10}Be ages of 6.1-9.0 Ma (Fig. 7b; Tables 1 and 2). Similarities in ^{10}Be concentration and age between samples in Cores 2-3 and those in Cores 18-20 suggest that the sediments from ~650 mbsf in the frontal prism may also correlate to the lower portion of the incoming Pacific sediment section. If so, this correlation implies that portions of the lower 50-100 m of the incoming Pacific Plate sediment section have been accreted during past stages of frontal prism formation, suggesting endmember models where the entire thickness of the incoming Pacific Plate sediment sequence can be accreted (Figs 3 a, d and e) may have been characteristic of this portion of the margin at times in the past.

4.2. Faults in the frontal prism

^{10}Be data from Site C0019 require at least six and as many as nine repetitions of low-over-high ^{10}Be concentration sediment (red arrows, Fig. 7b); at least one and up to three apparent stratigraphic omissions where there is an abrupt decrease in ^{10}Be concentration with depth (blue arrows in Fig. 7b); and two inverted sections where ^{10}Be concentrations increase with depth (grey arrows in Fig 7b). Each of these sequences is interpreted to indicate thrust faults, potential normal faults, and overturned sections, respectively (Fig. 5). In comparison, only one to three faults are required by the biostratigraphic age profile, and only two faults other than the décollement were identified by visual core description (Expedition 343/343T Scientists, 2013). These results show that ^{10}Be in deep marine sediments has the ability to provide higher chronological and spatial resolution than biostratigraphy alone and can be used to identify faulting at smaller scales, or in cores with incomplete recovery or fossil preservation.

Three known faults observed in cores from Site C0019 are associated with inversions and omissions in ^{10}Be concentrations (Fig. 7b and c). First, at 697 mbsf (Core 5R), a fault identified in the core by X-ray CT imaging is associated with a low over high ^{10}Be concentration inversion and a ^{10}Be inferred ~1.1 Ma difference in sediment age. Second, at 720 mbsf (Core 8R), a thrust fault observed in the core is associated with an overturned ^{10}Be section in the hanging wall of the thrust fault, consistent with the formation of a hanging wall anticline during imbricate thrusting. Third, across the plate boundary décollement, identified as an ~5 m-wide zone of scaly fabrics developed in smectite-rich clays in Core 17R (Expedition 343/343T Scientists, 2013), there is a two-order-of-magnitude decrease in ^{10}Be concentrations (10^9 to 10^7 atoms/g between Cores 16R and 18R). This change corresponds to an increase in ^{10}Be age from <1 Ma immediately above the décollement (819 mbsf) to 6-9 Ma below the décollement (825 mbsf). This observation is consistent with the décollement marking a major structural and lithologic boundary at Site C00019 (Expedition 343/343T Scientists, 2013).

Faults identified by ^{10}Be also correspond to structures inferred from Logging while drilling (LWD) resistivity images, fluid flow and thermal anomalies, and geochemically inferred faults (Fig. 7b and c). First, faults identified by ^{10}Be may correspond to fractures identified in LWD resistivity images at ~710, ~790, and ~820 mbsf (Expedition 343/343T Scientists, 2013), and thrust inversions interpreted from ^{10}Be data are associated with changes in bed dip direction determined from LWD resistivity images at ~760 mbsf, 795 and 828 mbsf (Fig. 7c). These data suggest some fractures identified in resistivity images may host fault offset, and are consistent with previous interpretations that changes in bedding dip direction may be associated with imbricate fault–and fault-related fold packages in the frontal prism (Chester and Moore, 2018; Expedition 343/343T Scientists, 2013). Second, three thermal anomalies at ~760, ~778, and ~810 mbsf, recorded by a thermistor string installed in the borehole, have been interpreted to result from fluid pulses along conductive fractures (Fulton & Brodsky, 2016). These depth ranges are associated with thrust and normal faults inferred from ^{10}Be data, and suggest that fluid flow may occur along discrete faults in the frontal prism. Third, trace element geochemistry in the sediment section below the décollement has been used to identify two additional faults at ~827 and ~832 mbsf (Rabinowitz et al., 2015). These geochemically inferred faults correspond to thrust inversions in the ^{10}Be data, and provide additional data to suggest the presence of multiple bedding parallel slip zones below the scaly clays interpreted to be the principal plate boundary shear zone (c.f. Kirkpatrick et al., 2015).

The ^{10}Be concentration profile from Site C0019, combined with structural, geophysical, and geochemical observations, collectively indicate a high density of faulting in the lower ~150 m of the frontal prism, with average fault spacing of ~10m (Fig. 7b). Because core recovery is <50% at site C0019, it is possible that many of the sections of intact core logged during Expedition 343 may be bound by fault zones that were not recovered due to poor cohesion and susceptibility to drilling-induced deformation. The decameter-scale stratal disruption suggested by ^{10}Be data is below the resolution of reflection seismic data across the prism, and may contribute to the seismically chaotic nature of the frontal prism (e.g., Nakamura et al., 2013).

5. Implications for sediment fluxes and décollement properties in the area of the 2011 Tohoku rupture

Comparison of meteoric ^{10}Be data from the frontal prism at IODP Site C0019, forearc slope at DSDP Site 434, and incoming plate at DSDP Site 456, provide new information on the evolution of the frontal prism and shallow décollement in a region of the northeast Japan plate boundary that hosted large magnitude tsunamigenic slip to the trench during the 2011 Tohoku event. In particular, these data can be used to infer: 1) the source of frontal prism sediments, 2) the relative roles of sediment accretion versus sediment subduction and 3) implications for the lithology and geometry of the shallow décollement.

Comparison of ^{10}Be concentrations from the frontal prism (Fig. 6b) to those in the forearc slope (Fig. 6a) and incoming plate (Fig. 6c) indicates that the lower prism is unlikely to be constructed from sediments isotopically similar to those in the forearc slope at Site 434, but requires a source from in the incoming plate. 0-2 Ma sediments (>8x10^{8} atoms/g ^{10}Be) in the frontal prism recovered at Site C0019 constitute ~70% of the measured samples above the décollement from ~640-820 mbsf (Fig. 6b). These ^{10}Be ages and concentrations overlap with those in the upper ~125 to 300 meters of sediment section at incoming reference site 436 (Fig. 6c), but are dissimilar to those at forearc slope site 434, where the majority of sediments are 2-4.5 Ma (3x10^{8} to 14x10^{8} atoms/g ^{10}Be), only ~10-20 m of 1-2 Ma sediments exist, and no sediments <1 Ma are present (Fig. 6a). Inputs from an ~2-4.5 Ma forearc slope section to the sampled portion of the lower prism are likely minimal, as material of this age and ^{10}Be concentration occur infrequently between ~640-820 mbsf at Site C0019 (Fig. 6a and b). It is possible that young sediments from the forerac slope have been gravitationally transported downslope and reworked into trench fill deposits that were subsequently accreted to the overriding plate. However, given the limited thickness and areal extent of young slope basin sediments relative to that on the incoming plate (~10-70 m at DSDP sites 435, 440, 441, 434, and 584; Barron et al., 1980; Niitsuma et al, 1986) reservoirs of young sediment available from the forearc slope are limited in comparison to those on the incoming plate. It is unlikely that gravitational or tectonic reworking of forearc slope materials alone could generate the volumes and age distributions of sediments observed at Site C0019, as would occur if the Japan trench were dominated by sediment subduction and tectonic erosion; rather the isotopic data appears to require accretion of incoming plate sediments (as depicted in Fig. 3d and e).

Active sediment accretion is also supported by the internal architecture of the prism. Thrust faults and overturned sections in the frontal prism, indicated by the ^{10}Be profile, are consistent with formation via imbricate thrusting (Fig. 3d and e) (Expedition 343/343T Scientists, 2013; Chester and Moore 2018). A major fault between 660 and 690 mbsf that places 6-9 Ma material over 1 Ma material, required by both biostratigraphic and ^{10}Be ages (Fig. 7b), could potentially be a thrust fault separating imbricate accreted sheets (Fig. 7c). An imbricate bounding fault at this stratigraphic horizon has also been interpreted by Chester and Moore (2018). The small-scale faulting observed in the prism and presence of faults inferred from ^{10}Be concentrations with both apparent thrust inversions and apparent normal omissions (Fig. 7b) are consistent with the predicted evolution of a frontal prism subject to repeated stages of internal deformation and slumping as the frontal prism is thrust over subducted horst and graben topography (Fig 3d).

Comparison of meteoric ^{10}Be data between the frontal prism and incoming reference site also place bounds on the volume and composition of subducted sediments at this location. The abundance of young 1-2 Ma sediments in the frontal prism indicates that accretion of at least the upper ~75-140 m of incoming plate sediment section must occur. The presence of ~4-9 Ma sediments recovered within the prism and the lack of sediments younger than ~6.7 Ma recovered below the décollement, suggest that at least some of the time, nearly the complete upper ~300 m of incoming section is accreted. These data imply that 50-100% of the thickness incoming section in the Japan trench can be accreted, which in turn implies that only 10-50% of the incoming sediment sequence may be subducted. Within the stratigraphic framework of the incoming section, the subducted materials include chert and pelagic clay, and, depending on accretion efficiency, the lowermost biogenic muds (Fig 2b).

The presence of late Pleistocene sediment immediately above the décollement requires that a portion of the frontal accretion at Site C0019 has occurred during the past ~100 Ka to ~1Ma. Given a convergence rate of ~80 km/Ma, the down-going plate from which this material was sourced has now been subducted to a position that is 8-80 km from the trench. This depth range is consistent with palinspastic reconstructions that suggest that young sediments immediately above the décollement were sourced ~9 km from the trench axis (Chester and Moore, 2018). These depth ranges overlap with the portion of the décollement that ruptured during the 2011 Tohoku earthquake, and in particular overlap with the shallow portion of plate boundary that hosted up to 50-60m of slip near the trench (Fig. 1). Therefore, the subducted sediments that escape accretion near Site C0019, chert, pelagic clay, basal biogenic muds, are the input sediments that provide host lithologies in which the décollement can localize in the near-trench region, and may host shallow tsunamigenic slip.

Additionally, ^{10}Be data suggest that plate boundary slip involves the development of faults at multiple stratigraphic and structural horizons. Below the décollement at Site C0019, ^{10}Be data indicate that the underthrust section is not in stratigraphic order, but contains at least one to two inversions of old-over-young material (Fig. 7b). This is consistent with interpretations by Kirkpatrick et al., (2015) (see their Fig. 9) and Rabinowitz et al., (2015) (see their Figs. 7 and Fig. 6), which suggest that at various points in time, additional fault surfaces may have accommodated plate boundary slip below the smectite-rich scaly shear zone at 821.5-822.5 mbsf identified as the plate boundary shear zone (Expedition 343/343T Scientists, 2013). Such a distributed zone of deformation, with multiple, subparallel to anastomosing faults within a shear zone, has also been predicted by numerical modeling of the plate boundary décollement (Koge et al., 2018). These data imply that the plate boundary décollement may have a complex evolutionary history with multiple detachment levels that can host slip near the trench. If any of these fault surfaces can host siesmogenic slip, as has been suggested by Rabinowitz et al., (*in review*), past Tohoku-like earthquakes may have propagated through either smectitite rich clays or biogenic muds, and future slip events may not necessarily reoccupy a principle slip surface from a previous event.

The volumes of accreted material and the internal architecture of the frontal prism help constrain the preferred stratigraphic level in which the décollement may develop in the Japan trench. Repetition of young, high ^{10}Be sediments suggests that at some points in time, the décollement may localize within the late Miocene to Quaternary biogenic muds (Fig 2b). However, the presence of sheared clays in the décollement, and the presence of >6-9 Ma sediments within the accretionary prism suggest that the plate boundary décollement may have a tendency to ultimately localize in the base of the biogenic muds, at or near the basal clays (Fig 2B). This idea is supported by high resolution seismic lines parallel and perpendicular to the Japan trench, and by palinspastic restorations based on seismic and core, which show décollement horizon developing directly above basaltic crust over both horsts and grabens (Chester and Moore 2018; Chester et al., 2013; Nakamura et al., 2013; Expedition 343/343T Scientists, 2013). Our data favor end member scenarios depicted in Figure 3d and e, which allow for partial to nearly complete sediment accretion, but are in consistent with endmember scenarios in Figures 3a, b, c, and f, which require nearly complete sediment subduction and / or frontal tectonic erosion. We suggest that frontal accretion at this site occurs by a combination of scenarios depicted in Figure 3b, d, and e, where the décollement may localize within he clays at the base of the incoming sediment section, in both horst and graben, at some points in time, while at other times the décollement may localize within the middle of the biogenic muds, particularly within graben.

Collectively these data imply that, even in the presence of subducted horst and graben topography, the décollement may be able to accrete sediments effectively, such that the contributions of sediment subduction or tectonic erosion are small. If true, the volume of subducted sediments that can contribute to fluid overpressures along the décollement, via compaction and dehydration, may be smaller than if the entire sequence was subducted (e.g. Kimura et al. 2012). This may limit the potential to which fluid overpressures generated by compaction and dewatering of the subducted sediment sequence could contribute to the nucleation or propagation of Tohoku–like events (c.f. Kimura et al., 2012). These data also imply that, while in the near-trench region, slip may occur within multiple lithologies, the décollement may ultimately develop in a stratigraphic horizon at or within low-friction, smectite-rich clays (e.g. Ikari et al, 2015) near the base of the incoming section, and that the décollement may have an undulating geometry that steps up and over horst and graben topography within the shallow portion of the subduction interface.

6. Conclusions

We use meteoric ^{10}Be in sediments recovered during IODP expedition 343 (JFAST) to quantify the age, architecture, and source of the frontal prism sediments in the Japan trench at a site where the plate boundary experienced slip to the trench during the 2011 Tohoku earthquake. These analyses demonstrate that meteoric ^{10}Be in deep marine sediments can be a viable tool to delineate the age, source, and structure of forearc sediments and constrain the structural history of frontal prisms, particularly in deep marine settings. Our data show that the frontal prism recovered at this location consists of relatively high ^{10}Be concentration, young sediments with more than half of the samples being <2 Ma. ^{10}Be data show pervasive apparent thrust and normal faulting that may be the result of imbrication, prism thickening, slumping, and extensional deformation during the subduction of horsts and grabens. The presence of thrust inversions of low-over-high-^{10}Be sediments below the décollement requires the presence of multiple faults within the plate boundary damage zone, some of which occur within the underthrust sediment sequence.

The ^{10}Be concentrations and ages determined for samples in the frontal prism above the décollement are similar to those in the upper ~125 to 300 of incoming Pacific Plate, but dissimilar to those in forearc slope sequence. These data suggest that the frontal prism at IODP Site C0019 are constructed largely of accreted sediment, with minimal input from recycled or reworked frontal slope sediments. The distribution of ^{10}Be concentrations and ages recovered at Site C0019 indicates that 50-90% of the incoming sediment sequence has been accreted over the past 1-2 Ma, and that the décollement is on average located at the base of, or in the lower half of the incoming sediment sequence. Collectively, these data imply that sediment accretion is relatively efficient, and that the décollement may preferentially be localized within or near smectite-rich clays located at the base of the incoming section even in the presence of subducted horst and graben topography. These data provide insight into the geometry and evolution of the frontal prism and shallow décollement in a portion of the northern Japan margin known to host large-magnitude seismogenic slip to the trench.

7. Acknowledgments, Samples, and Data

Funding for this work provided by the US Science Support Program Post Expedition Awards for IODP Expedition 343. Data supporting the conclusions can be obtained in Tables 1 through 3, and in cited references. Shipboard data from IODP Expedition 343 and DSDP Legs 56 & 57 can be accessed at http://sio7.jamstec.go.jp, http://publications.iodp.org, https://www.ngdc.noaa.gov, and http://deepseadrilling.org. The authors would like to thank Fred Chester and Makoto Otsubo, who provided careful reviews that greatly contributed to the manuscript, Kristin Morell, Christie Rowe, and Emily Schottenfels for edits to early versions of the manuscript, and the staff of the Scottish Universities Environmental Research Centre (SUERC) for support during accelerator mass spectrometry analyses.

8. References

Barron, J.A., Harper Jr, H.E., Keller, G., Reynolds, R.A., Sakai, T., Shaffer, B.L. and Thompson, P.R., 1980. Biostratigraphic summary of the Japan Trench transect, Legs 56 and 57, Deep Sea Drilling Project. *Langseth, M., Okada, H., et al., Init. Repts. DSDP*, *56*, p.57.

Brown, E. T., Edmond, J. M., Raisbeck, G. M., Bourlès, D. L., Yiou, F., & Measures, C. I. (1992). Beryllium isotope geochemistry in tropical river basins. *Geochimica et Cosmochimica Acta, 56*(4), 1607-1624.

Brown, L. (1987). ^{10}Be: Recent applications in Earth sciences. *Philosophical Transactions of the Royal Society of London. Series A, Mathematical and Physical Sciences, 323*(1569), 75-86.

Chase, Z., Anderson, R. F., Fleisher, M. Q., & Kubik, P. W. (2002). The influence of particle composition and particle flux on scavenging of Th, Pa and Be in the ocean. *Earth and Planetary Science Letters, 204*(1-2), 215-229.
Chester, F. M., Rowe, C., Ujiie, K., Kirkpatrick, J., Regalla, C., Remitti, F., et al. (2013). Structure and composition of the plate-boundary slip zone for the 2011 Tohoku-Oki earthquake. *Science, 342*(6163), 1208-1211.
Chester, F.M. and Moore, J.C., 2018. Tectonostratigraphy and processes of frontal accretion with horst-graben subduction at the Japan Trench. *Geology and Tectonics of Subduction Zones: A Tribute to Gaku Kimura*, *534*, p.101.
Clift, P. D., & Vannucchi, P. (2004). Controls on tectonic accretion versus erosion in subduction zones: Implications for the origin and recycling of the continental crust. *Review of Geophysics, 42*, 1-31.
Expedition 343/343T Scientists, (2013). Integrated Ocean Drilling Program Expedition 343/343T Preliminary Report, Japan Trench Fast Drilling Project (JFAST), 1 April –24 May 2012 and 5-19 July 2012. In *Integrated Ocean Drilling Project Preliminary Report* (Vol. 343).
Fulton, P. M., & Brodsky, E. E. (2016). In situ observations of earthquake-driven fluid pulses within the Japan Trench plate boundary fault zone. *Geology, 44*(10), 851-854.
Ikari, M. J., Kameda, J., Saffer, D. M., & Kopf, A. J. (2015). Strength characteristics of Japan Trench borehole samples in the high-slip region of the 2011 Tohoku-Oki earthquake. *Earth and Planetary Science Letters*, *412*, 35-41.
Kimura, G., Hina, S., Hamada, Y., Kameda, J., Tsuji, T., Kinoshita, M., & Yamaguchi, A. (2012). Runaway slip to the trench due to rupture of highly pressurized megathrust beneath the middle trench slope: The tsunamigenesis of the 2011 Tohoku earthquake off the east coast of northern Japan. *Earth and Planetary Science Letters, 339–340*(0), 32-45.
Kirkpatrick, J. D., Rowe, C. D., Ujiie, K., Moore, J. C., Regalla, C., Remitti, F., et al. (2015). Structure and lithology of the Japan Trench subduction plate boundary fault. *Tectonics, 34*(1), 53-69.
Kodaira, S., Fujie, G., Nakamura, Y., Obana, K., & Miura, S. (2017). *Seismological character of the incoming plate to the Japan Trench and its implication for seismogenic processes.* Paper presented at the EGU General Assembly Conference Abstracts.
Koge, H., Yamada, Y., Ohde, A., Bauville, A., Yamaguchi, A., & Ashi, J. (2018). Dynamic formation process of thick deformation zone on the shallow plate boundary fault of the Japan Trench: insight from analog experiments of half-graben subduction. *Progress in Earth and Planetary Science, 5*(1), 69.
Ku, T., Southon, J., Vogel, J., Liang, Z., Kusakabe, M., & Nelson, D. (1985). 10Be distributions in deep sea drilling project site 576 and site 578 sediments studied by accelerator mass spectrometry. *Initial Rep. Deep Sea Drill. Proj, 86*, 539-546.
Lay, T., Ammon, C., Kanamori, H., Xue, L., & Kim, M. (2011). Possible large near-trench slip during the great 2011 Tohoku (Mw 9.0) earthquake. *Earth Planets Space*.
Lao, Y., Anderson, R. F., Broecker, W. S., Trumbore, S. E., Hofmann, H. J., & Wolfli, W. (1992). Transport and burial rates of10Be and231Pa in the Pacific Ocean during the Holocene period. *Earth and Planetary Science Letters*, *113*(1-2), 173-189.
Luo, S., & Ku, T.-L. (2004). On the importance of opal, carbonate, and lithogenic clays in scavenging and fractionating 230Th, 231Pa and 10Be in the ocean. *Earth and Planetary Science Letters, 220*(1-2), 201-211.
McHargue, L., & Damon, P. (1991). The global beryllium 10 cycle. *Reviews of Geophysics, 29*(2), 141-158.
Measures, C., & Edmond, J. (1983). The geochemical cycle of ^{9}Be: a reconnaissance. *Earth and Planetary Science Letters, 66*, 101-110.
Morgan, J. K., Ramsey, E. B., & Ask, M. V. (2007). Deformation and mechanical strength of sediments at the Nankai subduction zone. The Seismogenic Zone of Subduction Thrust Faults, 210-256.

Mori, J., Chester, F. M., Eguchi, N., & Toczko, S. (2012). Integrated Ocean Drilling Program Expedition 343 Scientific Prospectus: Japan Trench Fast Earthquake Drilling Project (JFAST): Integrated Ocean Drilling Program Management International. *Inc.*.

Morris, J., Gosse, J. C., Brachfeld, S., & Tera, F. (2002). Cosmogenic Be-10 and the Solid Earth: Studies in Geomagnetism, Subduction Zone Processes, and Active Tectonics. *Reviews in Mineralolgy*, 207-270.

Morris, J., Valentine, R., & Harrison, T. (2002). Be-10 imaging of sediment accretion and subduction along the northeast Japan and Costa Rica convergent margins. *Geological Society of America Bulletin, 30*(1), 59-62.

Nakamura, Y., Kodaira, S., Miura, S., Regalla, C., & Takahashi, N. (2013). High-resolution seismic imaging in the Japan Trench axis area off Miyagi, northeastern Japan. *Geophysical Research Letters, 40*(9), 1713-1718.

Niitsuma, N., 1986. 8. Mangetostratigraphy and Diatom Biostratigraphy of Site 584, Deep Sea Drilling Project Leg 87, and Implications for the Tectonic Evolution of the Japanese Island.

Niitsuma, N., 2004. Japan Trench and tectonics of the Japanese island arcs. *Island Arc*, *13*(1), pp.306-317.

Nishiizumi, K., Imamura, M., Caffee, M. W., Southon, J. R., Finkel, R. C., & McAninch, J. (2007). Absolute calibration of ^{10}Be AMS standards. *Nuclear Instruments and Methods in Physics Research Section B: Beam Interactions with Materials and Atoms, 258*(2), 403-413.

Rabinowitz, H. S., Savage, H. M., Plank, T., Polissar, P. J., Kirkpatrick, J. D., & Rowe, C. D. (2015). Multiple major faults at the Japan Trench: Chemostratigraphy of the plate boundary at IODP Exp. 343: JFAST. *Earth and Planetary Science Letters, 423*, 57-66.

Raisbeck, G., Yiou, F., Fruneau, M., Loiseaux, J., & Lieuvin, M. (1979). ^{10}Be concentration and residence time in the ocean surface layer. *Earth and Planetary Science Letters, 43*(2), 237-240.

Ruff, L. (1989). Do trench sediments affect great earthquake occurrence in subduction zones? *Pure and Applied Geophysics, 129*, 263-282.

Saffer, D. M., & Bekins, B. A. (2006). An evaluation of factors influencing pore pressure in accretionary complexes: Implications for taper angle and wedge mechanics. *Journal of Geophysical Research, 111*(B4), B04101. http://dx.doi.org/10.1029/2005JB003990

Saffer, D. M., & Tobin, H. J. (2011). Hydrogeology and mechanics of subduction zone forearcs: Fluid flow and pore pressure. *Annual Review of Earth and Planetary Sciences*, *39*, 157-186.

Seno, T., Stein, S. and Gripp, A.E., 1993. A model for the motion of the Philippine Sea plate consistent with NUVEL-1 and geological data. *Journal of Geophysical Research: Solid Earth*, *98*(B10), pp.17941-17948.

Scholl, D. W., von Huene, R., Vallier, T. L., & Howell, D. G. (1980). Sedimentary masses and concepts about tectonic processes at underthrust ocean margins. *Geology, 8*(12), 564.

Stone, J. (1998). A rapid fusion method for separation of beryllium-10 from soils and silicates. *Geochimica et Cosmochimica Acta, 62*(3), 555-561.

Underwood (Ed.) (2007). *Sediment inputs to subduction zones: Why lithostratigraphy and clay mineralogy matter*: Columbia University Press.

von Huene, R., & Culotta, R. C. (1989). Tectonic erosion at the front of the Japan Trench convergent margin. *Tectonophysics, 160*(1-4), 75-90.

von Huene, R., & Lallemand, S. (1990). Tectonic erosion along the Japan and Peru convergent margins. *Geological Society of America Bulletin, 102*(6), 704-720.

von Huene, R., & Scholl, D. W. (1991). Observations at convergent margins concerning sediment subduction, subduction erosion, and the growth of continental crust. *Reviews of Geophysics, 29*(3), 279.

Wang, L., Ku, T. L., Luo, S., Southon, J. R., & Kusakabe, M. (1996). ^{26}Al-^{10}Be systematics in deep-sea sediments. *Geochimica et Cosmochimica Acta, 60*(1), 109-119.

Xu, S., Freeman, S. P., Rood, D. H., & Shanks, R. P. (2015). Decadal ^{10}Be, ^{26}Al and ^{36}Cl QA measurements on the SUERC 5 MV accelerator mass spectrometer. *Nuclear Instruments and*

Methods in Physics Research Section B: Beam Interactions with Materials and Atoms, *361*, 39-42.

You, C.-F., Morris, J., Gieskes, J., Rosenbauer, R., Zheng, S., Xu, X., et al. (1994). Mobilization of beryllium in the sedimentary column at convergent margins. *Geochimica et Cosmochimica Acta, 58*(22), 4887-4897.

Figure 1. Geologic setting of the study area. Digital elevation model of the northeast Japan forearc showing locations of IODP Expedition 343 (JFAST) Site C0019 and DSDP Legs 56/57 Sites 434 and 436. Simplified annotation of slip contours for the 2011 Tohoku Earthquake (after Iinuma et al., 2012), and convergence vector after Niitsuma 2004 and Seno et al. 1993.

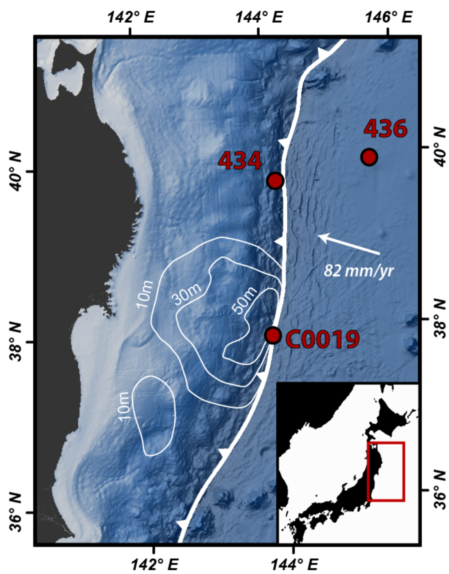

Figure 2. a. Simplified, schematic cross section showing the structure of the forearc at ~40°N (after Niitsuma, 2004). **b.** Simplified stratigraphic columns of sediment sections cored at DSDP Leg 56/57 Site 434 on the forearc slope, and Site 436 on the incoming plate. **c.** Simplified interpretation of high-resolution seismic line HS34B at the location of the JFAST Site C0019 (~38°N), showing the location of the plate boundary décollement, and imbrication of the incoming sediment section at the trench (after Nakamura et al., 2013).

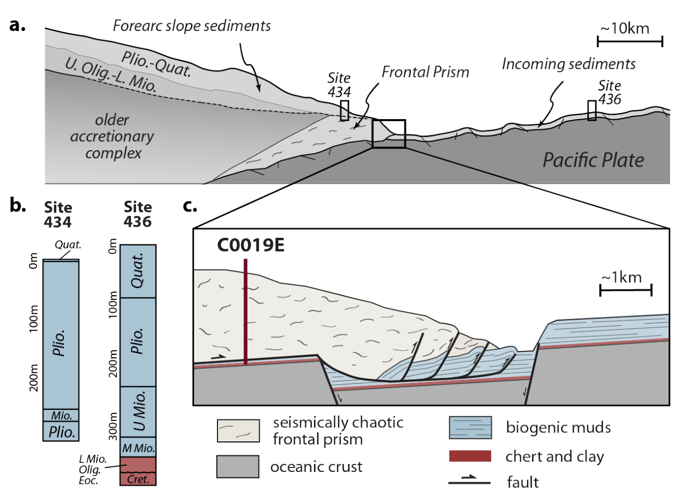

Figure 3. Schematic diagrams showing predicted concentrations of ^{10}Be in the frontal prism in endmember scenarios with: varying degrees of sediment accretion, sediment subduction, and frontal tectonic erosion. Scenarios presented for subduction of smooth seafloor topography and for horst and graben topography.

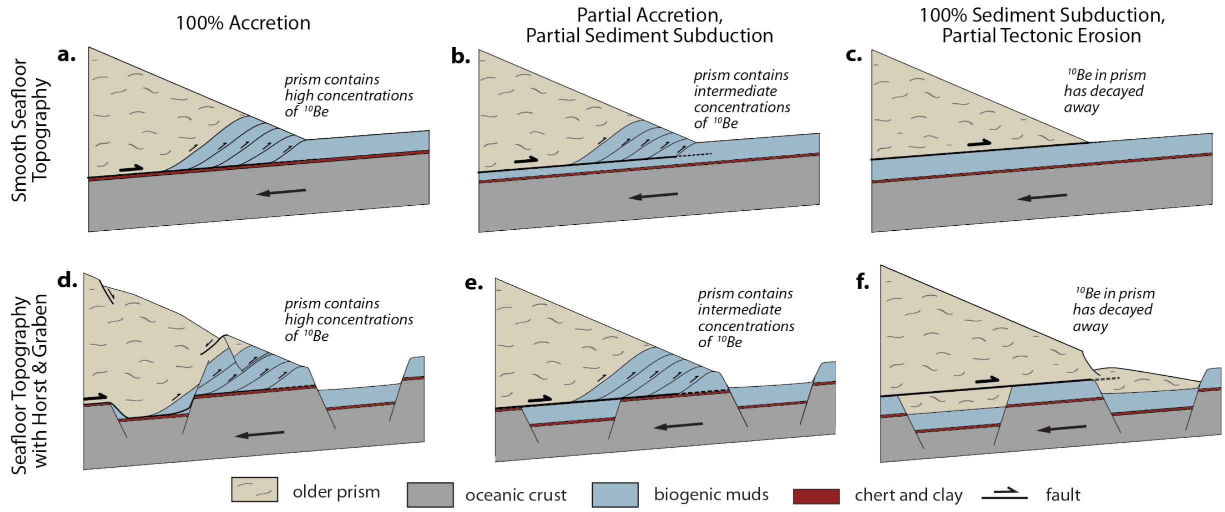

Figure 4. Schematic diagram showing how ^{10}Be produced in the atmosphere accumulates in marine sediments. The radio-decay of ^{10}Be after deposition results in an exponential decrease in concentration with depth.

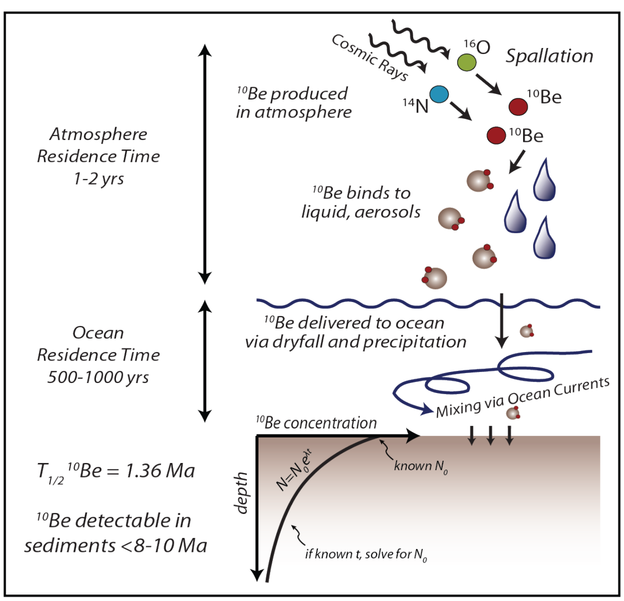

Figure 5. Idealized ^{10}Be depth profiles. (**a.**) An undisturbed stratigraphic section on the incoming plate that experienced continuous deposition at a continuous rate. (**b-d**) Sections where a stratigraphic sequence has been: (**b.**) repeated by a thrust fault, (**c.**) omitted by a normal fault, erosion, or depositional hiatus, or faulting of a folded section, or (**d.**) overturned by folding.

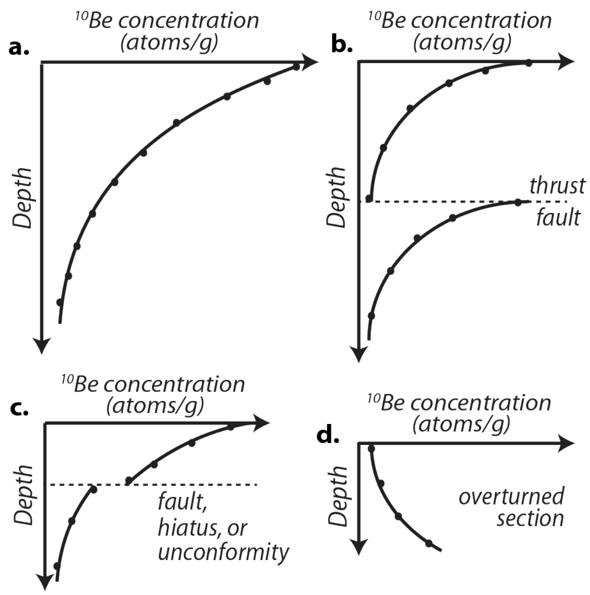

Figure 6. Comparison of ^{10}Be concentrations (bottom scale) and ^{10}Be ages (top scale) between (**a.**) forearc slope Site 434, (**b.**) frontal prism Site C0019, and (**c.**) incoming plate Site 436 (see Figs. 1 and 2 for locations). Numbers in parentheses are minimum and maximum ^{10}Be ages. Note the abundance of <1 and 1-2 Ma samples in forearc prism and incoming sediment sections, and a lack of equivalent section in forearc slope. Dashed line in (**b.**) represents the plate boundary décollement.

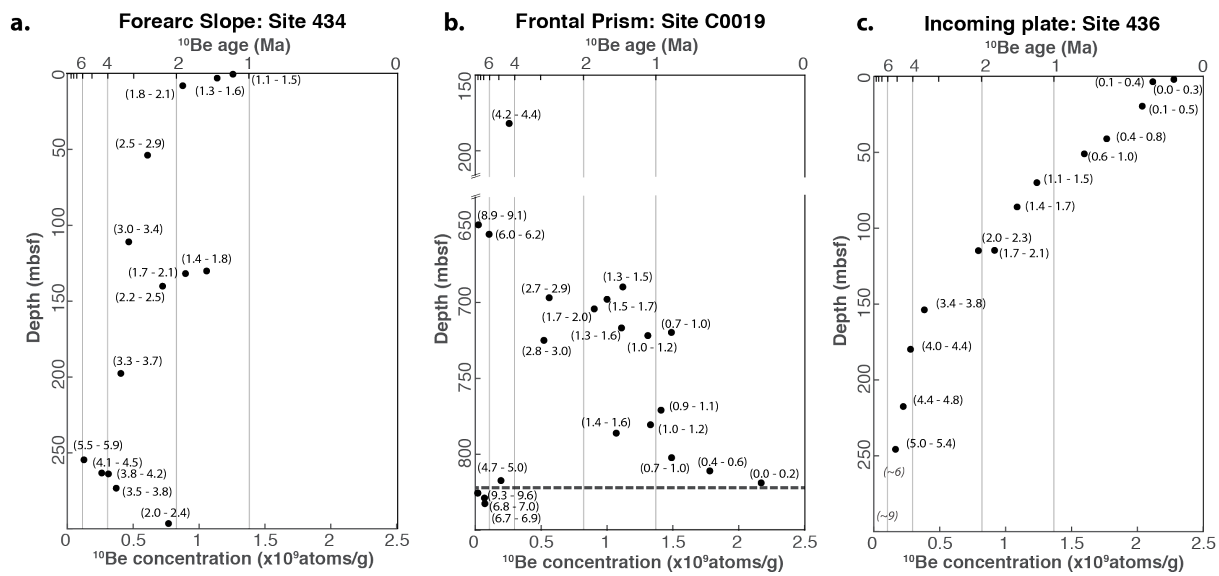

Figure 7. Comparison of faults identified from ^{10}Be concentration and ^{10}Be age data, to those identified by other methods. **A.** Log and Core Units from Site C0019, after Expedition 343/343T Scientists (2013). **B. Left:** ^{10}Be concentrations and **Right:** ^{10}Be ages, compared to Radiolarian biostratigraphic ages, for all samples from C0019. Faults and overturned sections inferred from ^{10}Be concentration profile are annotated with red, blue, and grey arrows. **C. Left:** Apparent bedding dips (red tabs) and faults (grey dashed arrows) inferred from LWD resistivity imagery. **Right:** Faults observed in core (labelled with apparent slip sense), fractures identified from LWD resistivity imagery, and faults inferred from fluid flow anomalies and geochemical inversions. a - Exp. 343 Scientists, 2013; b - Chester and Moore, 2018; c - Fulton and Brodsky, 2016; d - Rabinowitz et al., 2015.

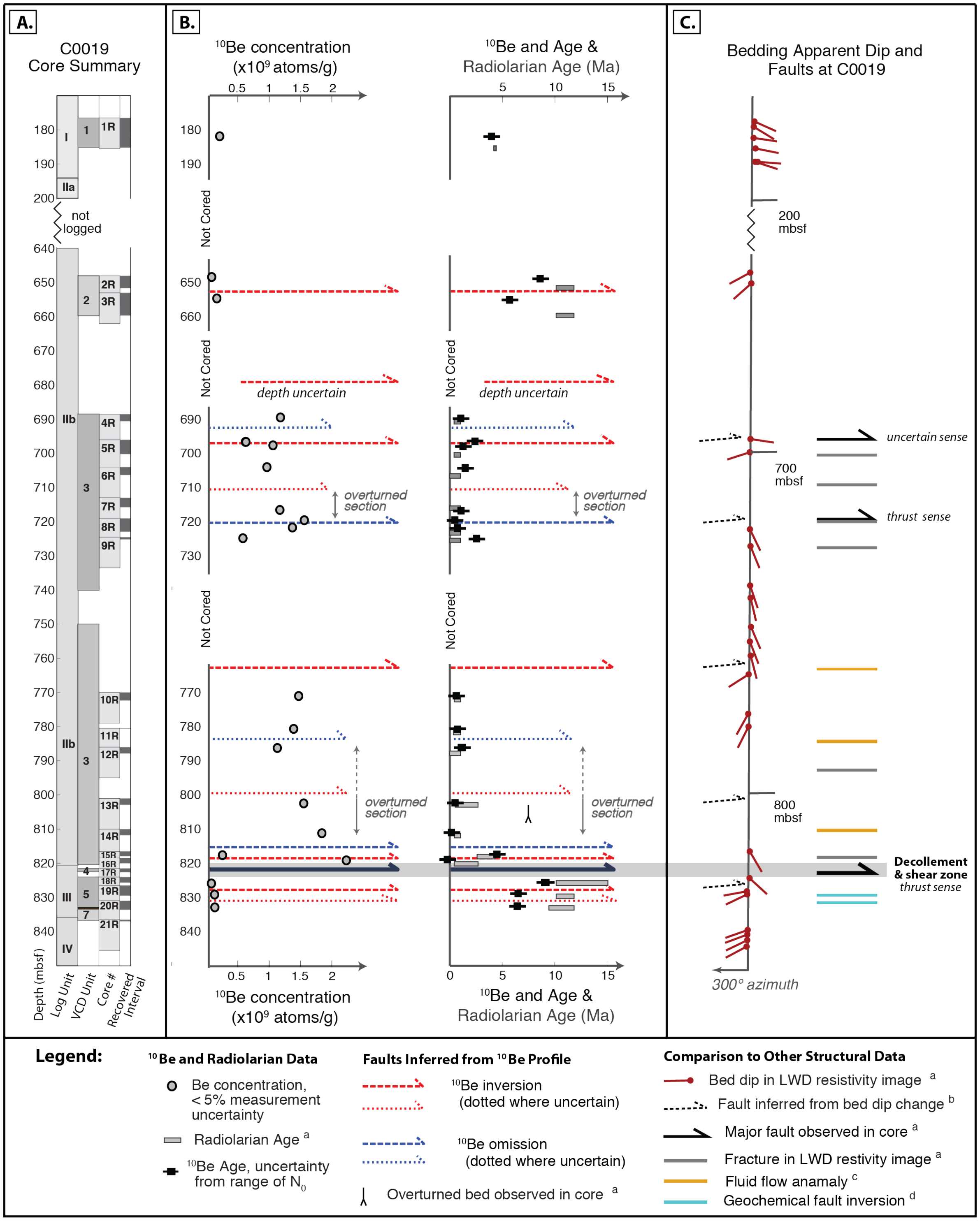
A.
C0019
Core Summary
not
logged
Depth (mbsf)
Log Unit
VCD Unit
Core #
Recovered Interval
B.
10Be concentration
(x10⁹ atoms/g)
10Be and Age &
Radiolarian Age (Ma)
Not Cored
depth uncertain
overturned
section
C.
Bedding Apparent Dip and
Faults at C0019
200
mbsf
700
mbsf
800
mbsf
uncertain sense
thrust sense
Decollement
& shear zone
thrust sense
300° azimuth
Legend:
10Be and Radiolarian Data
Be concentration,
< 5% measurement
uncertainty
Radiolarian Age a
10Be Age, uncertainty
from range of N0
Faults Inferred from 10Be Profile
10Be inversion
(dotted where uncertain)
10Be omission
(dotted where uncertain)
Overturned bed observed in core a
Comparison to Other Structural Data
Bed dip in LWD resistivity image a
Fault inferred from bed dip change b
Major fault observed in core a
Fracture in LWD restivity image a
Fluid flow anamaly c
Geochemical fault inversion d

Table 1. Meteoric ^{10}Be isotopic data from IODP Expedition 343, Site C0019 Hole E.

IODP Sample Interval	^{10}Be Sample Name	SUERC ID	depth (mbsf)	Sample mass (g)	^{9}Be carrier mass (μg)	Blank corrected ^{10}Be/^{9}Be ratio (x10^{-12})[a] ± 1σ uncertainty [b]	^{10}Be atoms/g (x10^{8})[a] ± 1σ uncertainty [b]
C0019E-1R-3, 128.0 cm	343-1-3	b6651	181.87	0.503	449.89	4.27 ± 0.03	2.55 ± 0.02
C0019E-2R-1, 83.0 cm	343-2-1	b6654	648.83	0.499	441.01	0.40 ± 0.01	0.24 ± 0.01
C0019E-3R-1, 102.0 cm	343-3-1	b6655	655.04	0.500	449.44	1.74 ± 0.02	1.05 ± 0.01
C0019E-4R-2, 2.0 cm	343-4-2	b6659	689.75	0.498	445.89	18.74 ± 0.07	11.21 ± 0.04
C0019E-5R-1, 43.0 cm	343-5-1 [c,d]	b6660	696.86	0.502	442.34	9.53 ± 0.07	5.61 ± 0.04
C0019E-5R-1, 43.0 cm	343-5-1 [c,d]	b6687	696.86	0.504	445.45	9.64 ± 0.08	5.69 ± 0.05
C0019E-5R-2, 24.0 cm	343-5-2	b6661	697.88	0.500	445.89	16.85 ± 0.06	10.04 ± 0.04
C0019E-6R-1, 11.0 cm	343-6-1	b6662	704.22	0.502	445.89	15.21 ± 0.07	9.03 ± 0.04
C0019E-7R-2, 131.0 cm	343-7-2	b6663	716.76	0.506	446.34	18.84 ± 0.08	11.10 ± 0.05
C0019E-8R-1, 35.0 cm	343-8-1A [d]	b6665	719.70	0.499	445.89	25.11 ± 0.08	14.99 ± 0.05
C0019E-8R-1, 35.0 cm	343-8-1A [d]	b6688	719.70	0.500	446.34	24.66 ± 0.09	14.70 ± 0.05
C0019E-8R-1, 140.0 cm	343-8-1B	b6674	721.80	0.501	445.89	22.10 ± 0.08	13.14 ± 0.05
C0019E-9R-1, 22.0 cm	343-9-1	b6675	724.94	0.500	444.56	8.78 ± 0.04	5.21 ± 0.03
C0019E-10R-1, 47.0 cm	343-10-1	b6679	770.94	0.500	447.23	23.54 ± 0.08	14.06 ± 0.05
C0019E-11R-CC, 3.0 cm	343-11-cc	b6680	780.56	0.498	446.34	22.16 ± 0.08	13.26 ± 0.05
C0019E-12R-1, 4.0 cm	343-12-1	b6681	786.08	0.500	446.34	17.93 ± 0.07	10.69 ± 0.04
C0019E-13R-1, 63.0 cm	343-13-1	b6682	802.26	0.496	446.34	24.85 ± 0.09	14.94 ± 0.05
C0019E-14R-1, 48.0 cm	343-14-1	b6683	810.96	0.496	445.45	29.62 ± 0.18	17.77 ± 0.11
C0019E-15R-1, 42.0 cm	343-15-1	b6666	817.34	0.505	441.90	3.34 ± 0.03	1.95 ± 0.02
C0019E-16R-1, 18.0 cm	343-16-1	b6667	818.86	0.502	445.01	36.67 ± 0.23	21.71 ± 0.13
C0019E-18R-1, 78.0 cm	343-18-1 [d]	b6668	825.56	0.504	444.12	0.31 ± 0.01	0.18 ± 0.00
C0019E-18R-1, 78.0 cm	343-18-1 [d]	b6689	825.56	0.505	445.89	0.33 ± 0.01	0.19 ± 0.01
C0019E-19R-1, 117.0 cm	343-19-1	b6669	828.84	0.500	441.90	1.18 ± 0.02	0.70 ± 0.01
C0019E-20R-2, 10.0 cm	343-20-2	b6673	832.52	0.501	449.89	1.21 ± 0.02	0.73 ± 0.01

a- Samples referenced to the NIST standard with an assumed ratio of 2.79x10^{-11} (Nishiizumi et al., 2007); measured ratios are blank corrected using laboratory blanks of 2.53x10^{-15} ± 8.01x10^{-16} and 7.25x10^{-15} ± 1.16x10^{-15}. Blank corrections were inconsequential, at <0.6% of the measured isotopic ratio.

b - AMS analytical uncertainties

c - low current

d - replicate measruement

Table 2. ^{10}Be ages for samples from IODP Expedition 343 Site C0019 Hole E.

IODP Sample Interval	^{10}Be Sample Name	Depth (mbsf)	Minimum ^{10}Be age (Ma) [a] ± 1σ analytical uncertainty	Maximum ^{10}Be age (Ma) [a] ± 1σ analytical uncertainty
C0019E-1R-3, 128.0 cm	343-1-3	181.87	4.20 ± 0.02	4.43 ± 0.02
C0019E-2R-1, 83.0 cm	343-2-1	648.83	8.87 ± 0.05	9.10 ± 0.05
C0019E-3R-1, 102.0 cm	343-3-1	655.04	5.95 ± 0.02	6.18 ± 0.02
C0019E-4R-2, 2.0 cm	343-4-2	689.75	1.30 ± 0.01	1.53 ± 0.01
C0019E-5R-1, 43.0 cm [b]	343-5-1	696.86	2.66 ± 0.01	2.88 ± 0.01
C0019E-5R-1, 43.0 cm [b]	343-5-1	696.86	2.63 ± 0.02	2.86 ± 0.02
C0019E-5R-2, 24.0 cm	343-5-2	697.88	1.51 ± 0.01	1.74 ± 0.01
C0019E-6R-1, 11.0 cm	343-6-1	704.22	1.72 ± 0.01	1.95 ± 0.01
C0019E-7R-2, 131.0 cm	343-7-2	716.76	1.32 ± 0.01	1.55 ± 0.01
C0019E-8R-1, 35.0 cm [b]	343-8-1A	719.70	0.73 ± 0.01	0.96 ± 0.01
C0019E-8R-1, 35.0 cm [b]	343-8-1A	719.70	0.76 ± 0.01	0.99 ± 0.01
C0019E-8R-1, 140.0 cm	343-8-1B	721.80	0.99 ± 0.01	1.21 ± 0.01
C0019E-9R-1, 22.0 cm	343-9-1	724.94	2.80 ± 0.01	3.03 ± 0.01
C0019E-10R-1, 47.0 cm	343-10-1	770.94	0.85 ± 0.01	1.08 ± 0.01
C0019E-11R-CC, 3.0 cm	343-11-cc	780.56	0.97 ± 0.01	1.20 ± 0.01
C0019E-12R-1, 4.0 cm	343-12-1	786.08	1.39 ± 0.01	1.62 ± 0.01
C0019E-13R-1, 63.0 cm	343-13-1	802.26	0.73 ± 0.01	0.96 ± 0.01
C0019E-14R-1, 48.0 cm	343-14-1	810.96	0.39 ± 0.01	0.62 ± 0.01
C0019E-15R-1, 42.0 cm	343-15-1	817.34	4.73 ± 0.02	4.96 ± 0.02
C0019E-16R-1, 18.0 cm	343-16-1	818.86	0.00 ± 0.01	0.23 ± 0.01
C0019E-18R-1, 78.0 cm [b]	343-18-1	825.56	9.41 ± 0.05	9.63 ± 0.05
C0019E-18R-1, 78.0 cm [b]	343-18-1	825.56	9.27 ± 0.05	9.50 ± 0.05
C0019E-19R-1, 117.0 cm	343-19-1	828.84	6.75 ± 0.03	6.98 ± 0.03
C0019E-20R-2, 10.0 cm	343-20-2	832.52	6.67 ± 0.03	6.90 ± 0.03

a - Assuming N_o = 2.17 to 2.44 $*10^9$ atm/g ^{10}Be

b - replicate measurement

Table 3. ^{10}Be concentrations from DSDP Legs 56 & 57 Sites 434 and 436[a].

IODP Sample Interval	Depth (mbsf)	Minimum ^{10}Be atoms/g ($x10^8$) ± 1σ uncertainty [b]	Maximim ^{10}Be atoms/g ($x10^8$) ± 1σ uncertainty [b]	Minimum ^{10}Be age ± 1σ uncertainty (Ma) [b]	Maximum ^{10}Be age ± 1σ uncertainty (Ma) [b]
DSDP Site 434					
434-1-1, 74-75 cm	0.74	11.90 ± 0.44	14.49 ± 0.44	1.07 ± 0.06	1.46 ± 0.07
434-1-3, 33-34 cm	3.3	10.83 ± 0.51	13.18 ± 0.56	1.26 ± 0.08	1.64 ± 0.09
434-2-2, 26-27 cm	8.3	8.33 ± 0.47	10.14 ± 0.53	1.77 ± 0.10	2.16 ± 0.11
434-7-1, 14-15 cm	54.1	5.79 ± 0.37	7.06 ± 0.42	2.48 ± 0.11	2.87 ± 0.12
434-13-cc, 21-22 cm	111.2	4.44 ± 0.31	5.40 ± 0.36	3.01 ± 0.13	3.39 ± 0.13
434-15-1, 40-42 cm	130.4	10.05 ± 0.77	12.24 ± 0.90	1.40 ± 0.14	1.79 ± 0.14
434-15-2,61-63 cm	132.1	8.53 ± 0.70	10.38 ± 0.82	1.72 ± 0.15	2.11 ± 0.15
434-16-1, 91-93 cm	140.4	6.87 ± 0.60	8.37 ± 0.71	2.15 ± 0.16	2.53 ± 0.16
434-22-1, 136-138 cm	197.9	3.87 ± 0.36	4.72 ± 0.42	3.27 ± 0.17	3.66 ± 0.17
434-28-1,130-132 cm	254.8	1.23 ± 0.12	1.49 ± 0.14	5.53 ± 0.18	5.92 ± 0.18
434-29-1,46-48 cm	263.5	2.50 ± 0.25	3.04 ± 0.30	4.13 ± 0.19	4.52 ± 0.19
434-29-1,109-111 cm	264.1	2.98 ± 0.32	3.63 ± 0.38	3.79 ± 0.19	4.17 ± 0.20
434-30-1,102-104 cm	273.5	3.54 ± 0.39	4.31 ± 0.47	3.45 ± 0.20	3.83 ± 0.21
434-33-2,80-82 cm	296.8	7.30 ± 0.83	8.89 ± 1.00	2.03 ± 0.21	2.41 ± 0.21
DSDP Site 436					
436-1-2, 70-71 cm	2.2	21.58 ± 0.96	26.28 ± 0.79	-0.10 ± 0.06	0.29 ± 0.09
436-1-3, 69-70 cm	3.7	20.05 ± 1.31	24.42 ± 1.04	0.05 ± 0.09	0.43 ± 0.13
436-3-2, 80-18 cm	19.8	19.27 ± 1.69	23.46 ± 1.22	0.12 ± 0.10	0.51 ± 0.18
436-5-4, 30-31 cm	41.3	16.80 ± 1.90	20.45 ± 1.23	0.39 ± 0.12	0.78 ± 0.24
436-6-4, 70-71 cm	51.2	15.14 ± 2.15	18.43 ± 1.24	0.60 ± 0.14	0.98 ± 0.30
436-8-4, 70-71 cm	70.2	11.71 ± 2.07	14.26 ± 1.05	1.10 ± 0.15	1.49 ± 0.38
436-10-2, 68-69 cm	86.2	10.28 ± 2.25	12.52 ± 0.99	1.36 ± 0.16	1.74 ± 0.48
436-13-2, 70-71 cm	114.8	8.71 ± 2.34	10.60 ± 0.90	1.68 ± 0.17	2.07 ± 0.61
436-13-2, 77-78 cm	115.0	7.54 ± 2.48	9.18 ± 0.83	1.96 ± 0.19	2.35 ± 0.78
436-17-3, 52-54 cm	154.0	3.66 ± 1.47	4.45 ± 0.42	3.39 ± 0.20	3.77 ± 1.01
436-20-1, 100-102 cm	180.0	2.66 ± 1.31	3.24 ± 0.32	4.01 ± 0.21	4.40 ± 1.33
436-24-1, 70-72 cm	217.7	2.14 ± 1.28	2.61 ± 0.27	4.43 ± 0.22	4.82 ± 1.79
436-27-1, 40-42 cm	245.9	1.58 ± 1.15	1.92 ± 0.21	5.03 ± 0.22	5.42 ± 2.57

a - after Morris et al. (2002)

b - Minimum and maximum bounds on ^{10}Be concentration and ^{10}Be age given corrections for the range of possible AMS standards used during intial AMS data collection. Calculated for NIST (SRM4325), LLNL 31000, LLSL 10000, LLNL 3000, LLNL 10000, and LLNL 300.

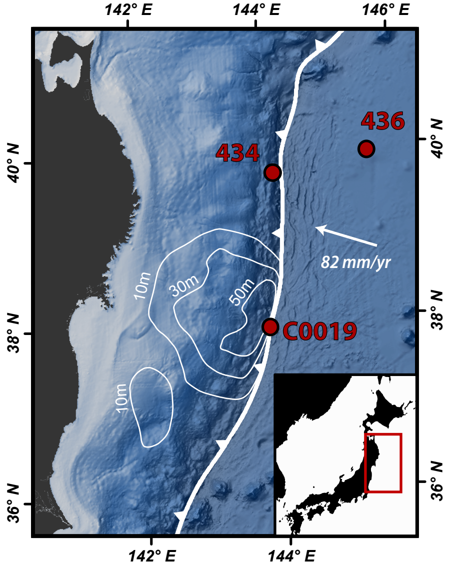
142° E
144° E
146° E
40° N
38° N
36° N
434
436
C0019
82 mm/yr
10m
30m
50m
10m
142° E
144° E
40° N
38° N
36° N

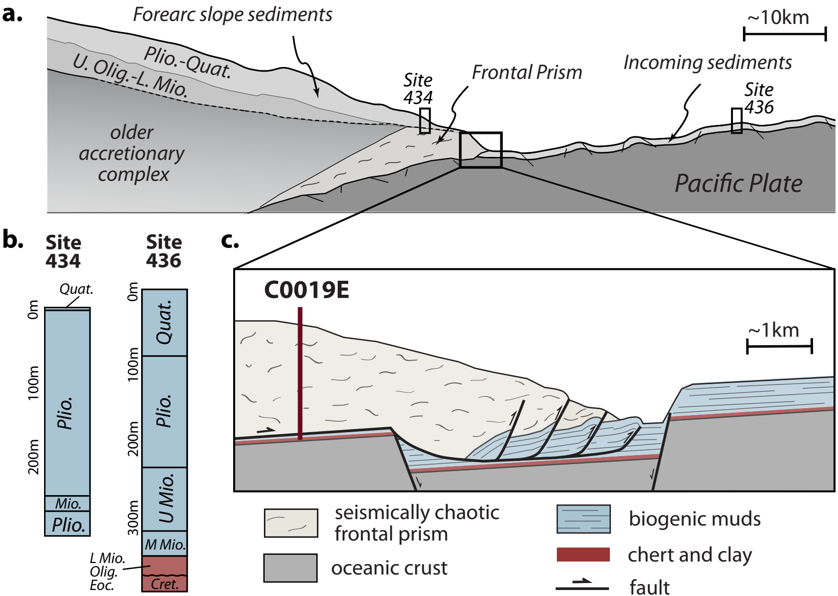
a.
Forearc slope sediments
~10km
Plio.-Quat.
U. Olig.-L. Mio.
Site 434
Frontal Prism
Incoming sediments
Site 436
older accretionary complex
Pacific Plate
b.
Site 434
Site 436
c.
Quat.
0m
100m
200m
300m
Plio.
Mio.
Plio.
Quat.
Plio.
U Mio.
M Mio.
L Mio.
Olig.
Eoc.
Cret.
C0019E
~1km
seismically chaotic frontal prism
oceanic crust
biogenic muds
chert and clay
fault

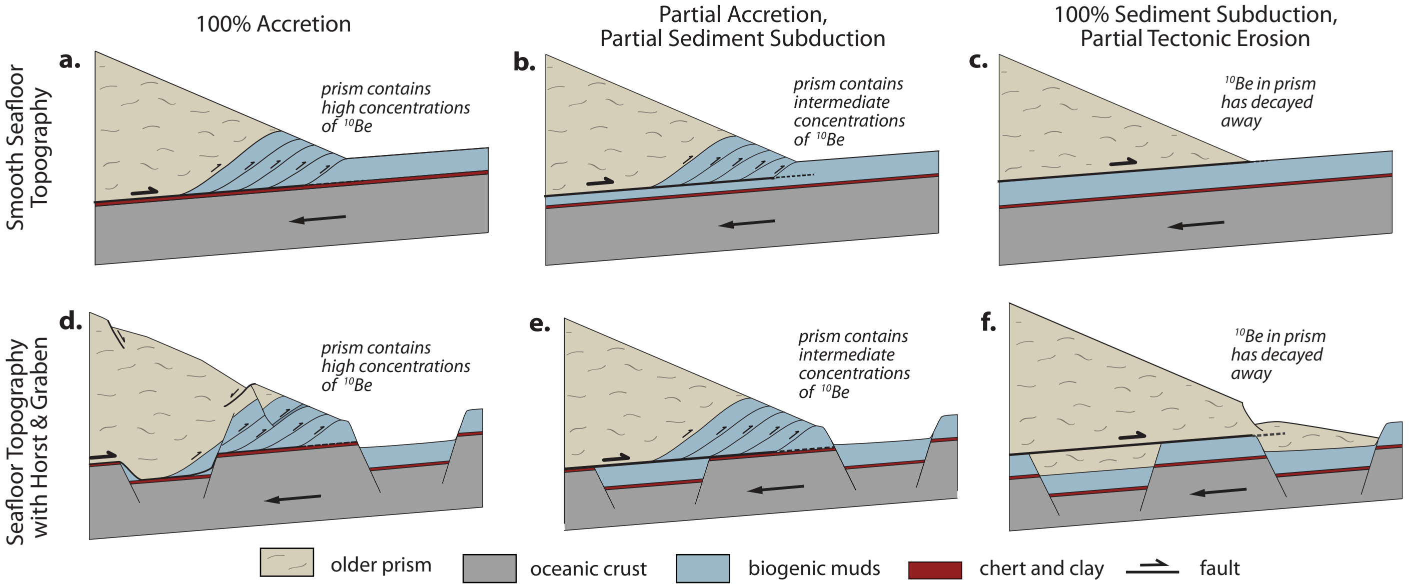
100% Accretion
Partial Accretion, Partial Sediment Subduction
100% Sediment Subduction, Partial Tectonic Erosion
Smooth Seafloor Topography
Seafloor Topography with Horst & Graben
a.
prism contains high concentrations of ^{10}Be
b.
prism contains intermediate concentrations of ^{10}Be
c.
^{10}Be in prism has decayed away
d.
prism contains high concentrations of ^{10}Be
e.
prism contains intermediate concentrations of ^{10}Be
f.
^{10}Be in prism has decayed away
older prism
oceanic crust
biogenic muds
chert and clay
fault

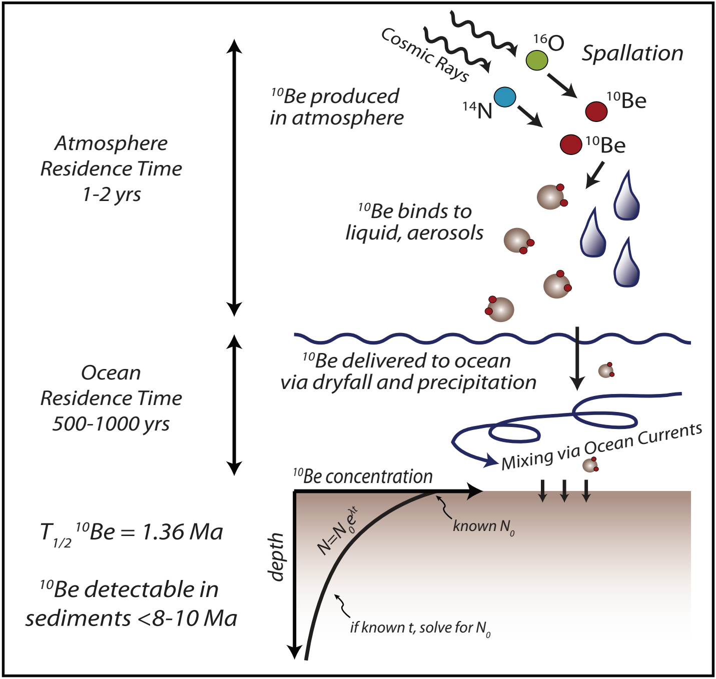
Cosmic Rays
16O
Spallation
10Be
14N
10Be
10Be produced
in atmosphere
Atmosphere
Residence Time
1-2 yrs
10Be binds to
liquid, aerosols
Ocean
Residence Time
500-1000 yrs
10Be delivered to ocean
via dryfall and precipitation
Mixing via Ocean Currents
10Be concentration
known N0
N=N0e-λt
depth
if known t, solve for N0
T1/2 10Be = 1.36 Ma
10Be detectable in
sediments <8-10 Ma

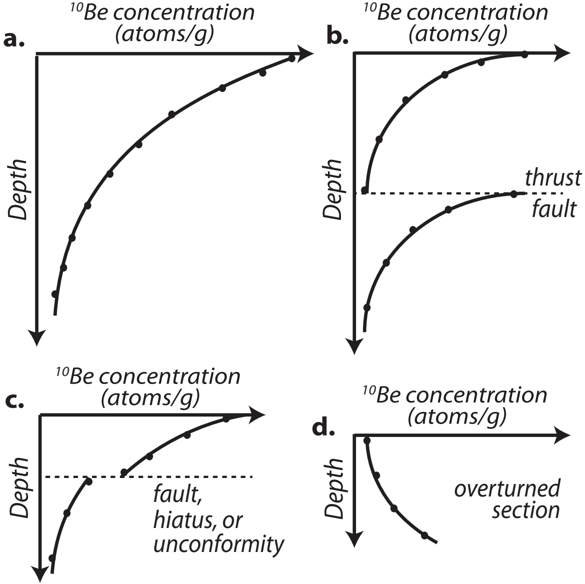
a.
^{10}Be concentration (atoms/g)
Depth
b.
^{10}Be concentration (atoms/g)
Depth
thrust
fault
c.
^{10}Be concentration (atoms/g)
Depth
fault,
hiatus, or
unconformity
d.
^{10}Be concentration (atoms/g)
Depth
overturned
section

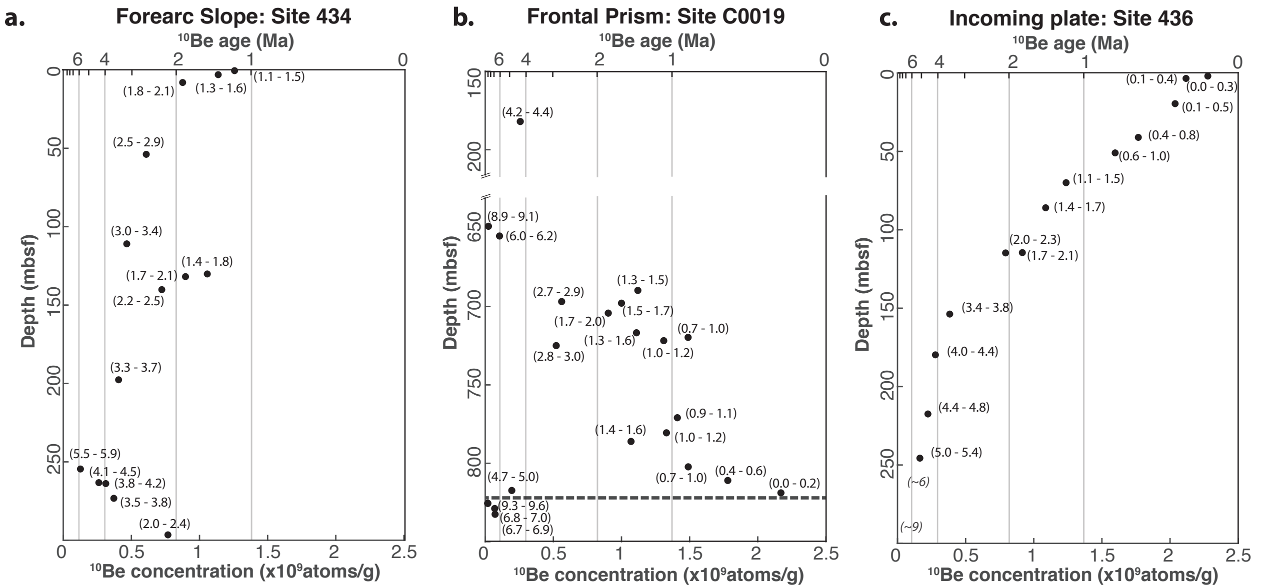
a.
Forearc Slope: Site 434
^{10}Be age (Ma)
Depth (mbsf)
^{10}Be concentration (x10^{9}atoms/g)
(1.1 - 1.5)
(1.3 - 1.6)
(1.8 - 2.1)
(2.5 - 2.9)
(3.0 - 3.4)
(1.4 - 1.8)
(1.7 - 2.1)
(2.2 - 2.5)
(3.3 - 3.7)
(5.5 - 5.9)
(4.1 - 4.5)
(3.8 - 4.2)
(3.5 - 3.8)
(2.0 - 2.4)
b.
Frontal Prism: Site C0019
^{10}Be age (Ma)
Depth (mbsf)
^{10}Be concentration (x10^{9}atoms/g)
(4.2 - 4.4)
(8.9 - 9.1)
(6.0 - 6.2)
(1.3 - 1.5)
(2.7 - 2.9)
(1.5 - 1.7)
(1.7 - 2.0)
(0.7 - 1.0)
(1.3 - 1.6)
(1.0 - 1.2)
(2.8 - 3.0)
(0.9 - 1.1)
(1.4 - 1.6)
(1.0 - 1.2)
(0.4 - 0.6)
(0.7 - 1.0)
(0.0 - 0.2)
(4.7 - 5.0)
(9.3 - 9.6)
(6.8 - 7.0)
(6.7 - 6.9)
c.
Incoming plate: Site 436
^{10}Be age (Ma)
Depth (mbsf)
^{10}Be concentration (x10^{9}atoms/g)
(0.1 - 0.4)
(0.0 - 0.3)
(0.1 - 0.5)
(0.4 - 0.8)
(0.6 - 1.0)
(1.1 - 1.5)
(1.4 - 1.7)
(2.0 - 2.3)
(1.7 - 2.1)
(3.4 - 3.8)
(4.0 - 4.4)
(4.4 - 4.8)
(5.0 - 5.4)
(~6)
(~9)

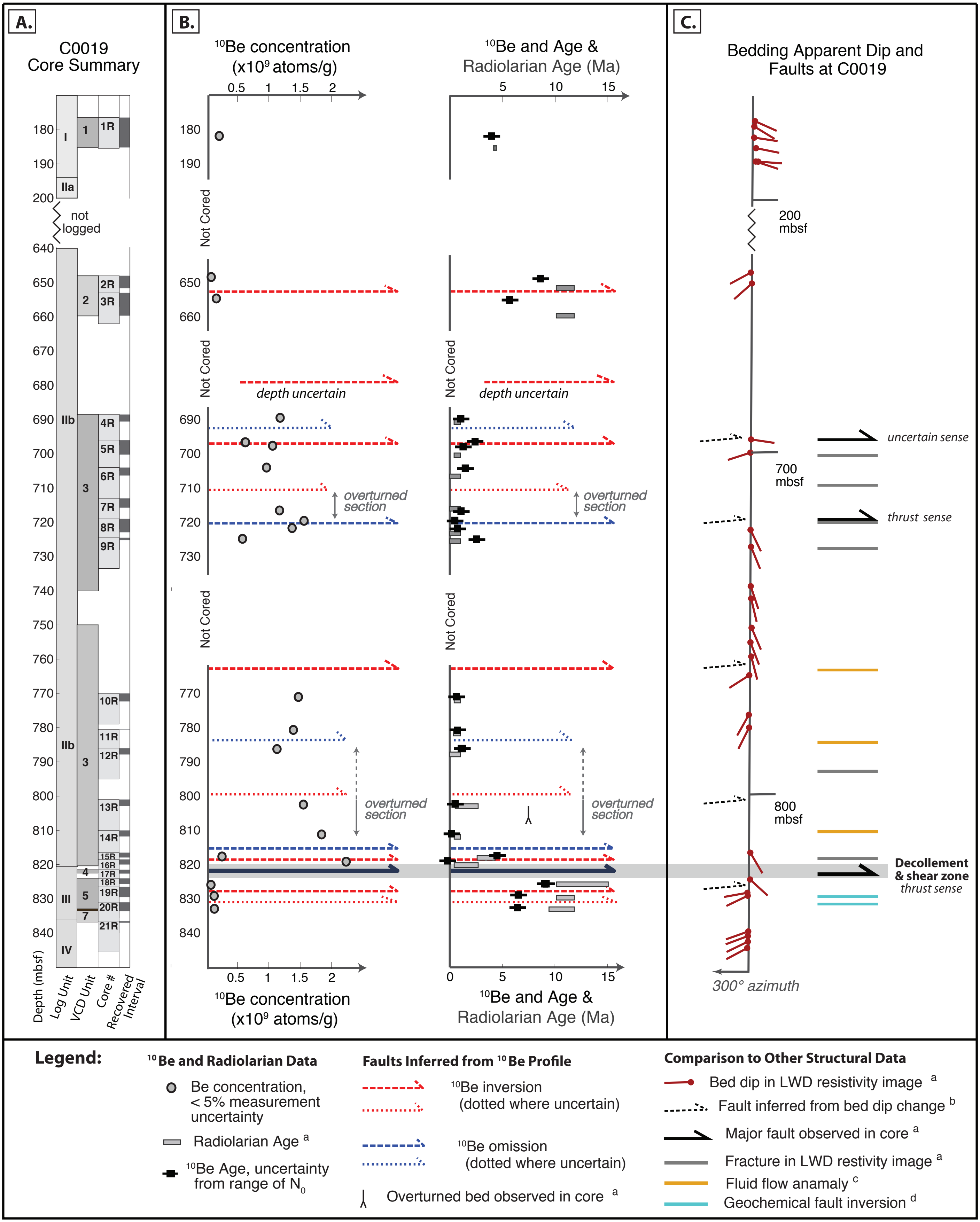

A.
C0019
Core Summary
not
logged
Depth (mbsf)
Log Unit
VCD Unit
Core #
Recovered Interval
I
IIa
IIb
III
IV
1R
2R
3R
4R
5R
6R
7R
8R
9R
10R
11R
12R
13R
14R
15R
16R
17R
18R
19R
20R
21R
B.
^{10}Be concentration
(x10^9 atoms/g)
^{10}Be and Age &
Radiolarian Age (Ma)
Not Cored
depth uncertain
overturned
section
C.
Bedding Apparent Dip and
Faults at C0019
200
mbsf
700
mbsf
800
mbsf
uncertain sense
thrust sense
Decollement
& shear zone
thrust sense
300° azimuth
Legend:
^{10}Be and Radiolarian Data
Be concentration,
< 5% measurement
uncertainty
Radiolarian Age [a]
^{10}Be Age, uncertainty
from range of N_0
Faults Inferred from ^{10}Be Profile
^{10}Be inversion
(dotted where uncertain)
^{10}Be omission
(dotted where uncertain)
Overturned bed observed in core [a]
Comparison to Other Structural Data
Bed dip in LWD resistivity image [a]
Fault inferred from bed dip change [b]
Major fault observed in core [a]
Fracture in LWD resistivity image [a]
Fluid flow anamaly [c]
Geochemical fault inversion [d]

Table 1: Meteoric 10Be isotopic data from Expedition 343, Site C0019

IODP Sample Interval	^{10}Be Sample Name	SUERC ID	depth (mbsf)	Sample mass (g)	^{9}Be carrier mass (μg)	Blank corrected ^{10}Be/^{9}Be ratio ($x10^{-12}$)[a] ± 1σ uncertainty [b]	^{10}Be atoms/g ($x10^{8}$)[a] ± 1σ uncertainty [b]
C0019E-1R-3, 128.0 cm	343-1-3	b6651	181.87	0.503	449.89	4.27 ± 0.03	2.55 ± 0.02
C0019E-2R-1, 83.0 cm	343-2-1	b6654	648.83	0.499	441.01	0.40 ± 0.01	0.24 ± 0.01
C0019E-3R-1, 102.0 cm	343-3-1	b6655	655.04	0.500	449.44	1.74 ± 0.02	1.05 ± 0.01
C0019E-4R-2, 2.0 cm	343-4-2	b6659	689.75	0.498	445.89	18.74 ± 0.07	11.21 ± 0.04
C0019E-5R-1, 43.0 cm	343-5-1 [c,d]	b6660	696.86	0.502	442.34	9.53 ± 0.07	5.61 ± 0.04
C0019E-5R-1, 43.0 cm	343-5-1 [c,d]	b6687	696.86	0.504	445.45	9.64 ± 0.08	5.69 ± 0.05
C0019E-5R-2, 24.0 cm	343-5-2	b6661	697.88	0.500	445.89	16.85 ± 0.06	10.04 ± 0.04
C0019E-6R-1, 11.0 cm	343-6-1	b6662	704.22	0.502	445.89	15.21 ± 0.07	9.03 ± 0.04
C0019E-7R-2, 131.0 cm	343-7-2	b6663	716.76	0.506	446.34	18.84 ± 0.08	11.10 ± 0.05
C0019E-8R-1, 35.0 cm	343-8-1A [d]	b6665	719.70	0.499	445.89	25.11 ± 0.08	14.99 ± 0.05
C0019E-8R-1, 35.0 cm	343-8-1A [d]	b6688	719.70	0.500	446.34	24.66 ± 0.09	14.70 ± 0.05
C0019E-8R-1, 140.0 cm	343-8-1B	b6674	721.80	0.501	445.89	22.10 ± 0.08	13.14 ± 0.05
C0019E-9R-1, 22.0 cm	343-9-1	b6675	724.94	0.500	444.56	8.78 ± 0.04	5.21 ± 0.03
C0019E-10R-1, 47.0 cm	343-10-1	b6679	770.94	0.500	447.23	23.54 ± 0.08	14.06 ± 0.05
C0019E-11R-CC, 3.0 cm	343-11-cc	b6680	780.56	0.498	446.34	22.16 ± 0.08	13.26 ± 0.05
C0019E-12R-1, 4.0 cm	343-12-1	b6681	786.08	0.500	446.34	17.93 ± 0.07	10.69 ± 0.04
C0019E-13R-1, 63.0 cm	343-13-1	b6682	802.26	0.496	446.34	24.85 ± 0.09	14.94 ± 0.05
C0019E-14R-1, 48.0 cm	343-14-1	b6683	810.96	0.496	445.45	29.62 ± 0.18	17.77 ± 0.11
C0019E-15R-1, 42.0 cm	343-15-1	b6666	817.34	0.505	441.90	3.34 ± 0.03	1.95 ± 0.02
C0019E-16R-1, 18.0 cm	343-16-1	b6667	818.86	0.502	445.01	36.67 ± 0.23	21.71 ± 0.13
C0019E-18R-1, 78.0 cm	343-18-1 [d]	b6668	825.56	0.504	444.12	0.31 ± 0.01	0.18 ± 0.00
C0019E-18R-1, 78.0 cm	343-18-1 [d]	b6689	825.56	0.505	445.89	0.33 ± 0.01	0.19 ± 0.01
C0019E-19R-1, 117.0 cm	343-19-1	b6669	828.84	0.500	441.90	1.18 ± 0.02	0.70 ± 0.01
C0019E-20R-2, 10.0 cm	343-20-2	b6673	832.52	0.501	449.89	1.21 ± 0.02	0.73 ± 0.01

a- Samples referenced to the NIST standard with an assumed ratio of $2.79x10^{-11}$ (Nishiizumi et al., 2007); measured ratios are blank corrected using laboratory blanks of $2.53x10^{-15} \pm 8.01x10^{-16}$ and $7.25x10^{-15} \pm 1.16x10^{-15}$. Blank corrections were inconsequential, at <0.6% of the measured isotopic ratio.

b - AMS analytical uncertainties

c - low current

d - replicate measruement

Table 2: ^{10}Be ages for samples from IODP Exp 343 Site C0019E

IODP Sample Interval	^{10}Be Sample Name	Depth (mbsf)	Minimum ^{10}Be age (Ma) [a] ± 1σ analytical uncertainty	Maximum ^{10}Be age (Ma) [a] ± 1σ analytical uncertainty
C0019E-1R-3, 128.0 cm	343-1-3	181.87	4.20 ± 0.02	4.43 ± 0.02
C0019E-2R-1, 83.0 cm	343-2-1	648.83	8.87 ± 0.05	9.10 ± 0.05
C0019E-3R-1, 102.0 cm	343-3-1	655.04	5.95 ± 0.02	6.18 ± 0.02
C0019E-4R-2, 2.0 cm	343-4-2	689.75	1.30 ± 0.01	1.53 ± 0.01
C0019E-5R-1, 43.0 cm [b]	343-5-1	696.86	2.66 ± 0.01	2.88 ± 0.01
C0019E-5R-1, 43.0 cm [b]	343-5-1	696.86	2.63 ± 0.02	2.86 ± 0.02
C0019E-5R-2, 24.0 cm	343-5-2	697.88	1.51 ± 0.01	1.74 ± 0.01
C0019E-6R-1, 11.0 cm	343-6-1	704.22	1.72 ± 0.01	1.95 ± 0.01
C0019E-7R-2, 131.0 cm	343-7-2	716.76	1.32 ± 0.01	1.55 ± 0.01
C0019E-8R-1, 35.0 cm [b]	343-8-1A	719.70	0.73 ± 0.01	0.96 ± 0.01
C0019E-8R-1, 35.0 cm [b]	343-8-1A	719.70	0.76 ± 0.01	0.99 ± 0.01
C0019E-8R-1, 140.0 cm	343-8-1B	721.80	0.99 ± 0.01	1.21 ± 0.01
C0019E-9R-1, 22.0 cm	343-9-1	724.94	2.80 ± 0.01	3.03 ± 0.01
C0019E-10R-1, 47.0 cm	343-10-1	770.94	0.85 ± 0.01	1.08 ± 0.01
C0019E-11R-CC, 3.0 cm	343-11-cc	780.56	0.97 ± 0.01	1.20 ± 0.01
C0019E-12R-1, 4.0 cm	343-12-1	786.08	1.39 ± 0.01	1.62 ± 0.01
C0019E-13R-1, 63.0 cm	343-13-1	802.26	0.73 ± 0.01	0.96 ± 0.01
C0019E-14R-1, 48.0 cm	343-14-1	810.96	0.39 ± 0.01	0.62 ± 0.01
C0019E-15R-1, 42.0 cm	343-15-1	817.34	4.73 ± 0.02	4.96 ± 0.02
C0019E-16R-1, 18.0 cm	343-16-1	818.86	0.00 ± 0.01	0.23 ± 0.01
C0019E-18R-1, 78.0 cm [b]	343-18-1	825.56	9.41 ± 0.05	9.63 ± 0.05
C0019E-18R-1, 78.0 cm [b]	343-18-1	825.56	9.27 ± 0.05	9.50 ± 0.05
C0019E-19R-1, 117.0 cm	343-19-1	828.84	6.75 ± 0.03	6.98 ± 0.03
C0019E-20R-2, 10.0 cm	343-20-2	832.52	6.67 ± 0.03	6.90 ± 0.03

a - Assuming $N_o = 2.17$ to $2.44 * 10^9$ atm/g ^{10}Be

b - replicate measurement

Table 3: ^{10}Be concentrations from DSDP Legs 56 & 57 Sites 434 and 436[a].

IODP Sample Interval	Depth (mbsf)	Minimum ^{10}Be atoms/g (x10^{8}) ± 1σ uncertainty [b]	Maximim ^{10}Be atoms/g (x10^{8}) ± 1σ uncertainty [b]	Minimum ^{10}Be age ± 1σ uncertainty (Ma) [b]	Maximum ^{10}Be age ± 1σ uncertainty (Ma) [b]
DSDP Site 434					
434-1-1, 74-75 cm	0.74	11.90 ± 0.44	14.49 ± 0.44	1.07 ± 0.06	1.46 ± 0.07
434-1-3, 33-34 cm	3.3	10.83 ± 0.51	13.18 ± 0.56	1.26 ± 0.08	1.64 ± 0.09
434-2-2, 26-27 cm	8.3	8.33 ± 0.47	10.14 ± 0.53	1.77 ± 0.10	2.16 ± 0.11
434-7-1, 14-15 cm	54.1	5.79 ± 0.37	7.06 ± 0.42	2.48 ± 0.11	2.87 ± 0.12
434-13-cc, 21-22 cm	111.2	4.44 ± 0.31	5.40 ± 0.36	3.01 ± 0.13	3.39 ± 0.13
434-15-1, 40-42 cm	130.4	10.05 ± 0.77	12.24 ± 0.90	1.40 ± 0.14	1.79 ± 0.14
434-15-2,61-63 cm	132.1	8.53 ± 0.70	10.38 ± 0.82	1.72 ± 0.15	2.11 ± 0.15
434-16-1, 91-93 cm	140.4	6.87 ± 0.60	8.37 ± 0.71	2.15 ± 0.16	2.53 ± 0.16
434-22-1, 136-138 cm	197.9	3.87 ± 0.36	4.72 ± 0.42	3.27 ± 0.17	3.66 ± 0.17
434-28-1,130-132 cm	254.8	1.23 ± 0.12	1.49 ± 0.14	5.53 ± 0.18	5.92 ± 0.18
434-29-1,46-48 cm	263.5	2.50 ± 0.25	3.04 ± 0.30	4.13 ± 0.19	4.52 ± 0.19
434-29-1,109-111 cm	264.1	2.98 ± 0.32	3.63 ± 0.38	3.79 ± 0.19	4.17 ± 0.20
434-30-1,102-104 cm	273.5	3.54 ± 0.39	4.31 ± 0.47	3.45 ± 0.20	3.83 ± 0.21
434-33-2,80-82 cm	296.8	7.30 ± 0.83	8.89 ± 1.00	2.03 ± 0.21	2.41 ± 0.21
DSDP Site 436					
436-1-2, 70-71 cm	2.2	21.58 ± 0.96	26.28 ± 0.79	-0.10 ± 0.06	0.29 ± 0.09
436-1-3, 69-70 cm	3.7	20.05 ± 1.31	24.42 ± 1.04	0.05 ± 0.09	0.43 ± 0.13
436-3-2, 80-18 cm	19.8	19.27 ± 1.69	23.46 ± 1.22	0.12 ± 0.10	0.51 ± 0.18
436-5-4, 30-31 cm	41.3	16.80 ± 1.90	20.45 ± 1.23	0.39 ± 0.12	0.78 ± 0.24
436-6-4, 70-71 cm	51.2	15.14 ± 2.15	18.43 ± 1.24	0.60 ± 0.14	0.98 ± 0.30
436-8-4, 70-71 cm	70.2	11.71 ± 2.07	14.26 ± 1.05	1.10 ± 0.15	1.49 ± 0.38
436-10-2, 68-69 cm	86.2	10.28 ± 2.25	12.52 ± 0.99	1.36 ± 0.16	1.74 ± 0.48
436-13-2, 70-71 cm	114.8	8.71 ± 2.34	10.60 ± 0.90	1.68 ± 0.17	2.07 ± 0.61
436-13-2, 77-78 cm	115.0	7.54 ± 2.48	9.18 ± 0.83	1.96 ± 0.19	2.35 ± 0.78
436-17-3, 52-54 cm	154.0	3.66 ± 1.47	4.45 ± 0.42	3.39 ± 0.20	3.77 ± 1.01
436-20-1, 100-102 cm	180.0	2.66 ± 1.31	3.24 ± 0.32	4.01 ± 0.21	4.40 ± 1.33
436-24-1, 70-72 cm	217.7	2.14 ± 1.28	2.61 ± 0.27	4.43 ± 0.22	4.82 ± 1.79
436-27-1, 40-42 cm	245.9	1.58 ± 1.15	1.92 ± 0.21	5.03 ± 0.22	5.42 ± 2.57

a - after Morris et al. (2002)

b - Minimum and maximum bounds on ^{10}Be concentration and ^{10}Be age given corrections for the range of possible AMS standards used during intial AMS data collection. Calculated for NIST (SRM4325), LLNL 31000, LLSL 10000, LLNL 3000, LLNL 10000, and LLNL 300.